

# Control System Design for a Hypersonic Entry Capsule

a project presented to  
The Faculty of the Department of Aerospace Engineering  
San José State University

in partial fulfillment of the requirements for the degree  
*Master of Science in Aerospace Engineering*

by

**Joshua T. Stokes**

May 2022

Approved by

Dr. Thomas Lombaerts  
Faculty Advisor



© 2021  
Joshua T. Stokes  
ALL RIGHTS RESERVED

ABSTRACT  
**Control System Design for a Hypersonic Re-entry Capsule**  
Joshua T. Stokes

The contents of this report describe the control system design for a deployable entry vehicle. Entry vehicles that are utilized for sample return missions are traditionally large and heavy systems, which significantly limits the payload carrying capability of the mission. The development of deployable entry vehicles with reduced volume and mass was established to solve this problem. However, there are still many challenges associated with controlling these vehicles. This is the motivation for the topic of this report. The following sections include a brief literature review of the problem at hand to provide some background information on the problem as well as how it has been solved in the past. Following this, the design and analysis for a control system solution is presented. The dynamics of the system are modeled using a six degree of freedom simulation that is used to analyze the control system performance. The simulation utilizes aerodynamic loads computed from a computational fluid dynamics analysis. The control system is designed utilizing dynamic inversion in the control law to deal with the nonlinearities in the system. Two dynamic inversion schemes are implemented and tested. The simulation results verify that the control system design using these schemes is an effective method of controlling the hypersonic re-entry vehicle.

### **Acknowledgements**

I would like to acknowledge all of those who supported me in my journey of life and in my academic career. This begins with my mother who raised me and ultimately made me the person that I am today. This also includes the many great teachers that I have had throughout my life that inspired me to pursue a career in aerospace engineering. Lastly, I would like to thank the faculty of San Jose State University for providing me with an opportunity to continue my education and further develop myself as an engineer. A special thanks goes to my project advisor, Dr. Thomas Lombaerts, for providing the guidance necessary for the completion of this project.

## Table of Contents

|       |                                    |    |
|-------|------------------------------------|----|
| 1     | Introduction.....                  | 1  |
| 1.1   | Motivation .....                   | 1  |
| 1.2   | Literature Review .....            | 2  |
| 1.3   | Project Proposal.....              | 6  |
| 1.4   | Methodology .....                  | 6  |
| 2     | System Modeling .....              | 8  |
| 2.1   | ADEPT Vehicle Solid Model.....     | 8  |
| 2.2   | Aerodynamic Analysis .....         | 11 |
| 2.2.1 | Mesh Analysis.....                 | 12 |
| 2.2.2 | Results.....                       | 13 |
| 2.3   | System Dynamics.....               | 17 |
| 3     | Control System Design .....        | 19 |
| 3.1   | Control System Architecture.....   | 19 |
| 3.2   | Dynamic Inversion Methodology..... | 19 |
| 3.3   | Guidance Law .....                 | 20 |
| 3.3.1 | Dynamic Inversion.....             | 21 |
| 3.3.2 | Angle Allocation.....              | 24 |
| 3.4   | Angle and Rate Controller.....     | 24 |
| 3.4.1 | Coordinate Transformation.....     | 25 |
| 3.4.2 | Dynamic Inversion.....             | 25 |
| 3.5   | Control Allocation.....            | 26 |
| 4     | Simulation Results .....           | 29 |
| 4.1   | Angle and Rate Controller.....     | 29 |
| 4.1.1 | Dynamic Inversion.....             | 29 |
| 4.1.2 | Rate Controller.....               | 32 |
| 4.1.3 | Angle Controller .....             | 34 |
| 4.2   | Guidance Law .....                 | 35 |
| 4.3   | Flight Condition Variation .....   | 39 |
| 4.4   | Parameter Uncertainty.....         | 41 |
| 5     | Conclusion & Recommendations ..... | 43 |

## List of Figures

|  |    |
|--|----|
| Figure 1 – Traditional aeroshell entry vehicle RCS design [3] .....                    | 2  |
| Figure 2 – SR-1 and LNA design concepts [6] .....                                      | 3  |
| Figure 3 – Dimensions of ADEPT SR-1 [8] .....  | 4  |
| Figure 4 – LNA vehicle with aerodynamic flap surfaces [1].....                         | 5  |
| Figure 5 – ADEPT vehicle solid model.....  | 8  |
| Figure 6 – ADEPT vehicle engineering drawings .....                                    | 9  |
| Figure 7 – Coordinate system definition.....   | 10 |
| Figure 8 – Control surface polarity .....  | 11 |
| Figure 9 – ANSYS simulation initial setup .....  | 12 |
| Figure 10 – Mesh sizing results .....  | 13 |
| Figure 11 – Simulation scaled residuals .....  | 14 |
| Figure 12 – Simulation drag coefficient .....  | 14 |
| Figure 13 – CFD simulation streamline results .....                                    | 15 |
| Figure 14 – ADEPT vehicle aerodynamic coefficients .....                               | 16 |
| Figure 15 – Flap one aerodynamic coefficients (zero angle of attack and sideslip)..... | 16 |
| Figure 16 – Entry vehicle coordinate frames and vector definition.....                 | 18 |
| Figure 17 – Control system block diagram.....  | 19 |
| Figure 18 – Guidance law block diagram .....   | 21 |
| Figure 19 – INDI filter frequency response.....  | 24 |
| Figure 20 – Angle and rate controller block diagram .....                              | 25 |
| Figure 21 – NDI test acceleration output.....  | 29 |
| Figure 22 – NDI test rate output .....   | 30 |
| Figure 23 – NDI test flap deflection angles .....                                      | 30 |
| Figure 24 – INDI test acceleration outputs .....                                       | 31 |
| Figure 25 – INDI test rate output.....   | 31 |
| Figure 26 – INDI test flap deflection angles.....                                      | 32 |
| Figure 27 – Rate control performance .....   | 33 |
| Figure 28 – Rate control test flap deflections .....                                   | 33 |
| Figure 29 – Angle control performance.....   | 34 |
| Figure 30 – Angle control test flap deflections.....                                   | 35 |
| Figure 31 – Guidance law response to constant inputs.....                              | 36 |
| Figure 32 – Angle response to constant guidance inputs.....                            | 36 |
| Figure 33 – Flap deflection angles for constant guidance input .....                   | 37 |
| Figure 34 – Guidance law response to ramp inputs.....                                  | 38 |
| Figure 35 – Angle response to guidance ramp inputs.....                                | 38 |
| Figure 36 – Flap deflection angles for guidance ramp input .....                       | 39 |
| Figure 37 – Flight condition variation test results .....                              | 40 |
| Figure 38 – Flight condition velocity and altitude profiles.....                       | 41 |
| Figure 39 – NDI parameter uncertainty test .....                                       | 42 |
| Figure 40 – INDI parameter uncertainty test .....                                      | 42 |

### List of Symbols

| Symbol        | Definition   | Units (SI)        |
|---------------|--|-------------------|
| $a$           | Altitude   | km                |
| $B$           | Control effectiveness matrix                           | dimensionless     |
| $B_{rot}$     | Bank angle rotation matrix                             | dimensionless     |
| $D$           | Drag force   | N                 |
| $e$           | Control error signal                                   | dimensionless     |
| $G$           | Effector blending matrix                               | dimensionless     |
| $g(z)$        | Gravitational force as a function of distance          | N                 |
| $I$           | Mass moment of inertia                                 | kg*m <sup>2</sup> |
| $L$           | Lift force   | N                 |
| $\mathcal{L}$ | Aerodynamic roll moment                                | Nm                |
| $\mathcal{M}$ | Aerodynamic pitch moment                               | Nm                |
| $M$           | Mach number  | dimensionless     |
| $\mathcal{N}$ | Aerodynamic yaw moment                                 | Nm                |
| $p$           | Angular velocity about body x axis                     | deg/s             |
| $q$           | Angular velocity about body y axis                     | deg/s             |
| $r$           | Angular velocity about body z axis                     | deg/s             |
| $S$           | Side Force   | N                 |
| $V$           | Velocity   | km/s              |
| $z$           | Distance from vehicle to Earth's center                | N                 |
|               |  |                   |
| Greek Symbols |  |                   |
| $\alpha$      | Angle of attack  | deg               |
| $\beta$       | Side-slip angle  | deg               |
| $\delta$      | Flap deflection angle                                  | deg               |
| $\gamma$      | Flight path angle                                      | deg               |
| $\lambda$     | Longitude  | deg               |
| $\nu$         | Virtual control input                                  | dimensionless     |
| $\sigma$      | Bank angle   | deg               |
| $\phi$        | Latitude   | deg               |
| $\xi$         | Heading angle  | deg               |
|               |  |                   |
| Subscripts    |  |                   |
| $()_0$        | Refers to previous time step in control algorithm      |                   |
| $()_{cs}$     | Refers to control surfaces                             |                   |
| $()_v$        | Refers to vehicle without control surface contribution |                   |
| $()_x$        | Refers to the vehicle x-axis                           |                   |
| $()_y$        | Refers to the vehicle y-axis                           |                   |
| $()_z$        | Refers to the vehicle z-axis                           |                   |
| $()_l$        | Refers to lift   |                   |
| $()_d$        | Refers to drag   |                   |
| $()_s$        | Refers to side force                                   |                   |
|               |  |                   |

|          |   |  |
|----------|---|--|
| Acronyms |   |  |
| ADEPT    | Adaptable, Deployable, Entry and Placement Technology |  |
| CFD      | Computational Fluid Dynamics                          |  |
| DEV      | Deployable Entry Vehicle                              |  |
| DRM      | Design Reference Mission                              |  |
| ECEF     | Earth-Centered Earth-Fixed                            |  |
| HIAD     | Hypersonic Inflatable Aerodynamic Decelerator         |  |
| IMU      | Inertial Measurement Unit                             |  |
| INDI     | Incremental Nonlinear Dynamic Inversion               |  |
| LNA      | Lifting Nano ADEPT                                    |  |
| LQR      | Linear Quadratic Regulator                            |  |
| NDI      | Nonlinear Dynamic Inversion                           |  |
| RCS      | Reaction Control System                               |  |



# 1 Introduction

## 1.1 Motivation

Atmospheric re-entry vehicles safely deliver payloads through the hypersonic descent phase of a mission. These systems allow for the landing of payloads on other planets as well as safely returning samples through Earth's atmosphere. Traditionally, this is accomplished using rigid aeroshell-type vehicles. The increased effort to develop systems capable of delivering higher mass payloads has led to the development of entry vehicles that can be stowed throughout the mission and deployed during the atmospheric entry phase. These systems are referred to as Deployable Entry Vehicles (DEVs) and have reduced volume and mass when compared to traditional rigid aeroshell vehicles [1]. These reductions in volume and mass allow for larger and heavier payloads to be transported, furthering the capabilities of space exploration and sample return missions. These factors make the DEV systems a promising endeavor in the aerospace community.

A challenge that arises in the utilization of the DEV systems is in the control of the system during atmospheric entry. Traditional rigid aeroshell systems utilize thrusters attached to the vehicle to control the attitude during the descent. Since the DEV systems do not have rigid surfaces to which thrusters can be attached, this option is not easily implemented. There is the option of unguided descent, but this greatly reduces the accuracy of the landing ellipse that can be achieved. According to reference [2], the unguided descents of the Mars Pathfinder and Mars Exploration Rovers resulted in landing ellipses of "299 km x 45 km and 70 km x 5 km, respectively". Whereas the guided descent of the Mars Science Laboratory resulted in a landing ellipse of "approximately 20 x 7 km". This presents a significant improvement in the landing accuracy, providing sufficient motivation for the development of active control for DEV systems.

The method of control to be utilized is the use of articulated aerodynamic flaps to control the entry vehicle during descent. This methodology has been assessed for DEV systems in previous studies [1][3], which provide evidence that it is a viable method of controlling the vehicle. This provides some confidence in the method, while also providing a benchmark for the design. The control system design developed in this report differs from previous studies by making use of Nonlinear Dynamic Inversion (NDI) and Incremental Nonlinear Dynamic Inversion (INDI). Nonlinear Dynamic Inversion is a proven method of controlling nonlinear systems and INDI is an adaptation that offers unique benefits. To assess the effectiveness of these methods, both methods are implemented and the system performance is compared. The advantages provided by the use of these dynamic inversion methods can potentially offer improved control system performance of the aerodynamic flap system for DEV vehicles.

The motivation for the development of the DEV systems is driven by the desire for higher payload carrying capacity into the atmosphere. This development leads to the necessity of robust control systems capable of controlling the descent of the vehicle and improving the landing accuracy. These are the drivers for the development of an aerodynamic flap control system that utilizes the dynamic inversion control methods.

## 1.2 Literature Review

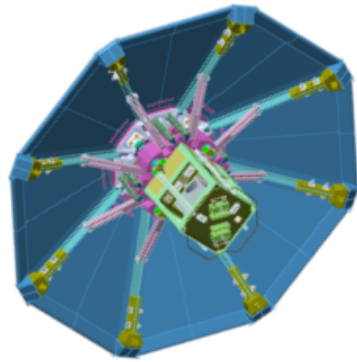
Reference [2] describes the control method for traditional rigid aeroshell systems. These systems have a hard back shell that can be utilized to attach reaction control system (RCS) thrusters. These thrusters can be fired to control the attitude of the vehicle during the descent phase. An example diagram of this system, taken from reference [3], is shown in Figure 1. While this approach is a sufficient method of controlling the vehicle, the completely rigid structure causes it to suffer from multiple drawbacks. These drawbacks include the additional mass, as well as the volume constraint of the launch vehicle. It is for these reasons, that the DEV systems were developed.



Figure 1 – Traditional aeroshell entry vehicle RCS design [3]

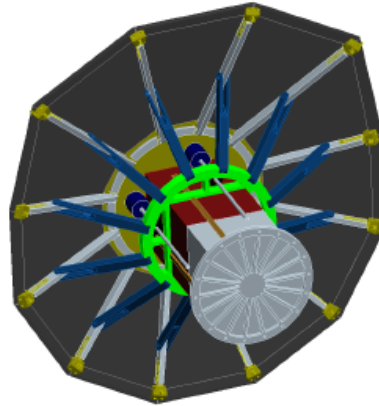
A NASA white paper providing an overview of the current DEV technology is provided in reference [5]. Two main types of DEV systems are described in the document. These systems are the Hypersonic Inflatable Aerodynamic Decelerator (HIAD), and the Adaptable, Deployable, Entry and Placement Technology (ADEPT) vehicle. The primary difference between the two systems is that the HIAD is deployed by inflating the aeroshell structure, and the ADEPT system is mechanically deployed. Another key difference documented in the reference is that the HIAD vehicle can be controlled by using actuators to morph the shape of the structure, thus affecting the force distribution on the surface. This means that developing an additional flap control method for the HIAD system is unnecessary. Thus, the control system design in this report will focus on the mechanically deployed ADEPT system.

The ADEPT vehicle concept will serve as the basis for the control design in this study. An overview of the vehicle concept is presented in [6]. The overall structure of the vehicle consists of a carbon fabric system stretched out in an umbrella-type shape across a number of stowable ribs. This allows for the vehicle to be folded up when not in use, greatly reducing the space taken up by the vehicle. When deployed, the woven carbon fabric provides thermal protection for the payload. There are two vehicle concepts for the ADEPT vehicle presented in reference [6], these are the SR-1 and the Lifting Nano ADEPT (LNA). The two design concepts from reference [6] are presented in Figure 2 below. For the control design presented in this paper, the SR-1 vehicle concept was used as the basis for a DEV vehicle design.



#### **SR-1 Features**

- 0.7m deployed diameter
- 8 ribs, 70 deg symmetric shape
- 4 layer carbon fabric system
- Unguided, ballistic entry
- Sounding rocket payload
  - 125 km apogee (Mach 3 peak)
  - Negligible aerothermal heating
- Simple, dual spring deployment system
- Free fall, ground impact, on-board data recovery



#### **LNA Features**

- 1.0m+ deployed diameter
- 12 ribs, 70 deg asymmetric shape with trim tab
- 6 layer carbon fabric system
- $L/D = 0.19$  ( $AoA = 11$  deg), Guided hypersonic flight
- LEO Secondary payload (ULA Centaur ABC)
  - 7.6 km/s entry from LEO (Mach 27 peak)
  - Aerothermal heating ( $>100$  W/cm<sup>2</sup>, 3.5 kJ/cm<sup>2</sup>)
- Electro-mechanical deployment system
- Parachute terminal descent, air-snatch recovery

Figure 2 – SR-1 and LNA design concepts [6]

Multiple studies support the performance of the ADEPT system. Reference [7] presents a wind tunnel study to examine the effects of aeroloads on the ADEPT design. This included the analysis of shape deflection, aeroelastic behavior, and aerodynamic forces and moments. One important finding from this study, according to the text is that “no flutter/buzz of the fabric was observed for any test condition” [7]. The effects of flutter can potentially be picked up by an inertial measurement unit (IMU) sensor and be fed back into the control system, affecting the performance of the controller. The experiments in this report also demonstrate the “capability of ADEPT to generate aerodynamic lift without the need for a center of gravity offset” [7]. Having a center of gravity (CG) aligned with the geometric center of the vehicle simplifies the control system design.

Reference [8] presents test results for a subscale ADEPT vehicle. For this test, a 50% geometric scale model of the SR-1 design was tested in the NASA Langley Research Center vertical spin tunnel. In addition to the testing procedures and results, this reference presents detailed geometry and physical properties for the full-scale SR-1 design. The geometry is displayed in Figure 3 below and the relevant physical properties are presented in Table 1. The geometry presented in Figure 3 will be used as the baseline for developing a model of the ADEPT vehicle for the analysis presented in this report. Additionally, the mass and inertia properties in Table 1 will serve as the baseline properties for the analysis.

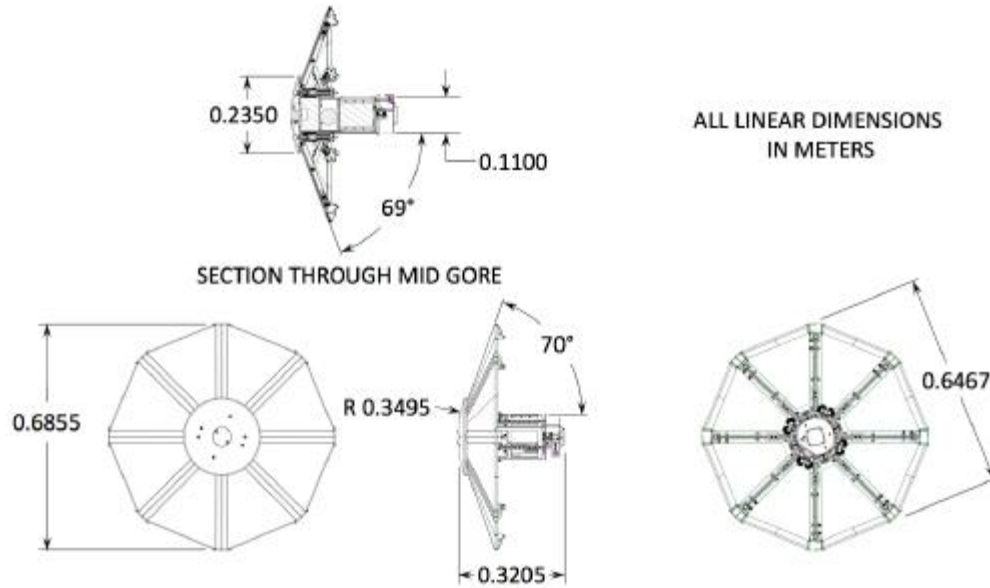


Figure 3 – Dimensions of ADEPT SR-1 [8]

Table 1 – Physical properties of ADEPT SR-1 [8]

| Property                                | Value                 |
|---|-----------------------|
| Maximum diameter (reference length) (m) | 0.700                 |
| Reference area (m <sup>2</sup> )        | 0.3849                |
| Center of mass location (mm)            | [-109.80, 0.25, 0.25] |
| Mass (kg)                               | 8.490                 |
| $I_{xx}$ (kg*m <sup>2</sup> )           | 0.2500                |
| $I_{yy}$ (kg*m <sup>2</sup> )           | 0.1722                |
| $I_{zz}$ (kg*m <sup>2</sup> )           | 0.1719                |

Reference [9] presents two design reference missions (DRMs) for the ADEPT system. These consist of a lunar return mission and a LEO return mission. The following initial conditions for these DRMs are provided: altitude, velocity, and flight path angle. The conditions for these DRMs that are provided in reference [9] are listed in Table 2 below. These parameters provide a realistic set of initial conditions to use as a starting point for the controls analysis to be conducted in this report.

Table 2 – ADEPT vehicle DRMs [9]

| Parameter      | Lunar Return | LEO Return |
|----------------|--------------|------------|
| a (km)         | 122          | 122        |
| V (km/s)       | 11.0         | 7.89       |
| $\gamma$ (deg) | -5.5         | -6.8       |

As mentioned previously, the control of the ADEPT vehicle using aerodynamic flaps has been assessed in previous studies [1][3]. The two referenced studies are a part of the Pterodactyl program, which is an effort to “advance the current state of the art for entry vehicle guidance and control” [1]. Additionally the two papers both focus on a flap control system design for the LNA

design concept, and follow similar methodologies. The papers begin by presenting the flap configurations to be utilized for the analysis. An example of this from reference [1] is shown in Figure 4 below. In this case, there are a total of eight hinged flaps that are attached to the ribs of the structure. The flaps are designed to be deflected to induce moments on the vehicle as the means of controlling it. By inspection of Figure 4, flaps 1,2,7, and 8 will primarily induce pitch torques and the remaining flaps will primarily induce yaw torques. The flaps are designed to stabilize the vehicle while also responding to angle of attack and sideslip angle commands that are generated by the guidance algorithm.

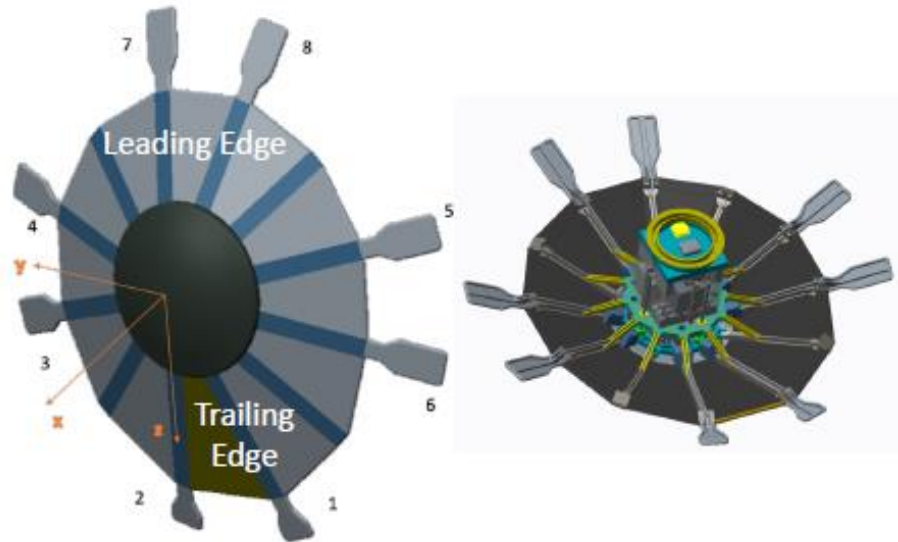


Figure 4 – LNA vehicle with aerodynamic flap surfaces [1]

References [1] and [3] also describe the methodology utilized to conduct the analysis. The simulation utilized to analyze the control system performance makes use of an aerodynamic database. This database is generated using computational fluid dynamics (CFD) analysis, and is comprised of the vehicle force and moment coefficients under different conditions. These conditions include Mach number, angle of attack, sideslip angle, and flap deflection angles. The generation of this database allows for the calculation of the forces and moments acting on the vehicle under any conditions through interpolation of the data. In addition to this, the modeling of the vehicle equations of motion are discussed. The entry vehicle equations of motion are taken from Vinh [10] and will be described in further detail later in this report. Lastly, the reference papers describe the design of the controller using the linear quadratic regulator methodology. The design of the controller is compiled into a simulation with the dynamic and kinematic models and used to assess the performance of the system. In both cases, it is shown that the aerodynamic flap control system is capable of effectively controlling the LNA vehicle throughout the descent into the atmosphere. The control system design and analysis presented in this report follows the modeling strategy described in references [1] and [3].

The control systems developed in references [1] and [3] both make use of an LQR controller design. For the control system design presented in this report, the dynamic inversion methodology is utilized instead. As mentioned in the previous section, INDI is an adaptation of the NDI method. NDI is described in detail in reference [11]. NDI-based control systems function by transforming the nonlinear dynamics equations into a form where the resulting

closed-loop plant dynamics function as a linear system. After transforming the plant into a linear form, traditional linear control methods can be utilized to generate the control inputs. This methodology is a useful method for nonlinear control, but it also relies heavily on modeling information in the control law. Thus, the controller becomes highly susceptible to errors caused by modeling uncertainties. A recommendation to remedy this issue is the use of the INDI methodology to increase the robustness to uncertainties.

INDI was created as a variation of NDI and was developed to decrease the controller dependency on the vehicle model, thereby increasing the robustness to uncertainties [4]. Thus, the INDI methodology provides the benefits of the NDI method while also reducing the drawbacks. Multiple sources support the usefulness of the methodology. Reference [4] describes the successful test flight of the method on the multi-rotor micro aerial vehicle. The report also expands this into a larger analysis of the method's utilization on full-sized aerial vehicles. An INDI control system is developed for a Cessna Citation and its performance and stability is analyzed showing the effectiveness of the controller. Furthermore, reference [12] analyzes the robustness of an INDI control system with regards to disturbance rejection, model uncertainties, and sensing perturbations. Additionally, it was found that "The INDI control method was proved to have better robust performance under regular perturbations as compared to NDI without using any robust or adaptive techniques" [12]. The results of these reports provide evidence that INDI controllers are feasible and worth investigating for the aerodynamic flap control design to deal with the nonlinear dynamics of the system.

This section has presented a review of the current literature on topics relevant to the problem at hand. This includes a look at the control methodology for traditional aeroshell entry vehicle designs to provide context on the problem. The design concept and properties for NASA's ADEPT vehicle are presented to provide a basis for a DEV vehicle concept to be modeled and utilized for analysis. The parameters for two potential ADEPT DRMs are also listed. Additionally, previous studies that assess the aerodynamic flap control design for these vehicles are discussed. These studies include information on modeling methodology as well as control system design. Lastly there is a discussion of the dynamic inversion control methods with references providing evidence to the feasibility and effectiveness of the methodology. The references discussed in this section provide the foundation for the analysis and design work performed in the following sections of the report.

### 1.3 Project Proposal

The objective of this project is to develop an aerodynamic flap actuated control system design for the ADEPT class entry vehicle. The developed control system shall be capable of stabilizing the vehicle throughout the descent phase and providing control over the vehicle angle of attack and sideslip angle to respond to guidance commands. Additionally, a guidance law will be developed to test closed-loop system performance. Performance of the controller shall be verified by utilizing computational models.

### 1.4 Methodology

A mathematical model of the system is developed using the equations of motion for a hypersonic entry capsule gathered from reference [10]. The aerodynamic force inputs to the model are determined by performing a CFD analysis on a generated 3D solid model of the

ADEPT vehicle. The CFD analysis is utilized to determine the aerodynamic forces and moments at different increments of angle of attack, sideslip angle, and flap deflection angles. The resulting data is be combined with the vehicle equations of motion to complete the mathematical model of the system and develop a simulation for the system dynamics

As mentioned in previous sections, the control system design utilizes the dynamic inversion methodology. Separate control laws are developed to make use of the NDI and INDI methods respectively. The mathematical model generated from the previous steps is be used to simulate and analyze the performance of the two inversion methods.

## 2 System Modeling

This section presents the steps taken to develop a high fidelity model of the re-entry system to be used for control system analysis. The modeling work includes the development of a solid model of the vehicle using CAD software. The solid model is utilized in CFD simulations to compute the aerodynamic forces and moments necessary for a system dynamics model. The aerodynamic forces and moments are compiled in a database that is then queried by a simulation that propagates the system equations of motion. These equations are defined in further detail in section 2.3.

### 2.1 ADEPT Vehicle Solid Model

A solid model for an ADEPT class DEV system was developed for utilization in a CFD analysis. The developed solid model includes the fully deployed DEV system as well as eight flap control surfaces. The dimensions for the model are based on the geometry provided in reference [8], which is shown on Figure 3. Figure 5 below presents a 3D image of the developed model. Figure 6 provides the 2D engineering drawings with the major dimensions labeled in meters.

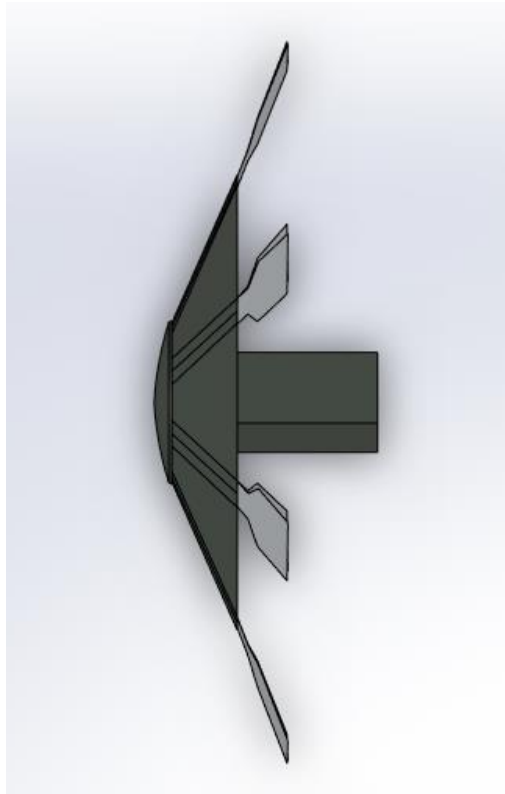


Figure 5 – ADEPT vehicle solid model



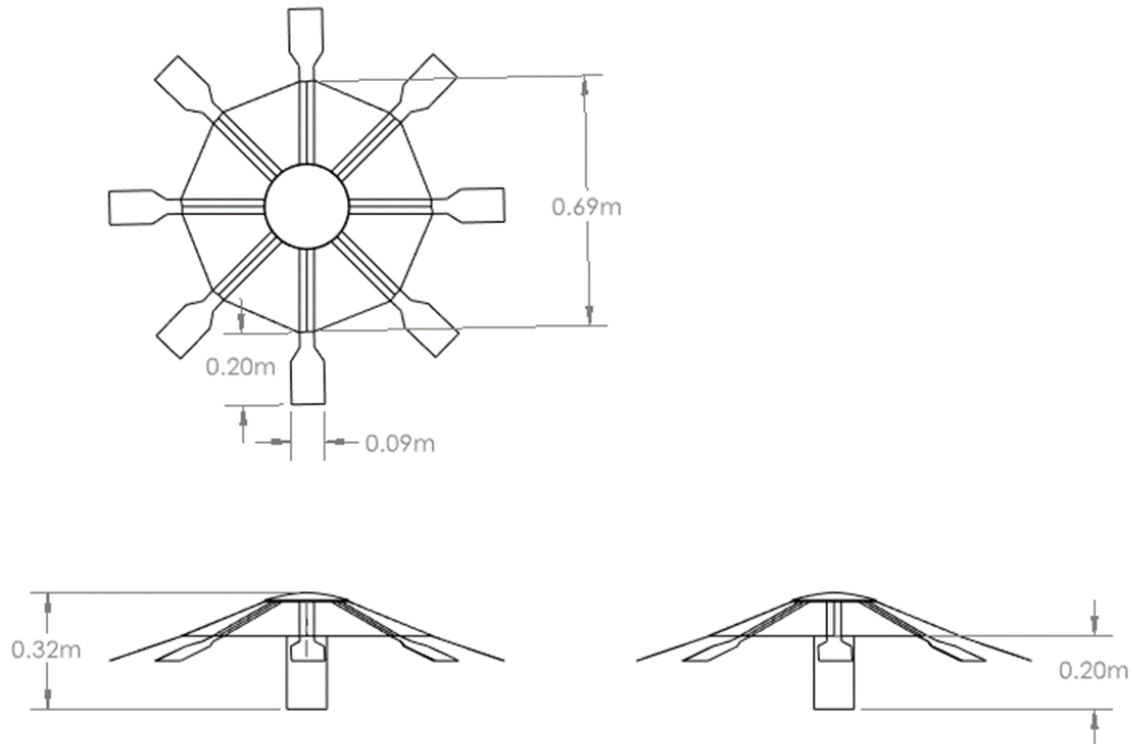


Figure 6 – ADEPT vehicle engineering drawings

Figure 7 below defines the body-fixed coordinate system used throughout the analysis. The origin of the coordinate system is centered at the front of the vehicle, in the center of the dome structure. The vehicle x-axis is defined through the centerline of the vehicle, with the positive direction pointing towards the front of the vehicle. The y-axis of the vehicle points through the right side of the vehicle. Lastly, the z-axis completes a right-handed coordinate system through a cross product between the x and y axes. The control surface flaps are defined in a counter-clockwise sequence starting from the positive y-axis. The flaps are shown at their zero degree deflection position, where they are aligned to the struts of the main vehicle structure.

The direction of the moments induced on the vehicle from the flaps can be determined via inspection of Figure 7. The flaps are placed such that they can be operated in pairs to provide uncoupled moments for the pitch (y) and yaw (z) axes. For example, by maneuvering flaps two and three by the same amount, a pitching moment will be generated but the net yaw moment will be zero. Table 3 summarizes the mapping between the flap numbers and the desired rotation axis.

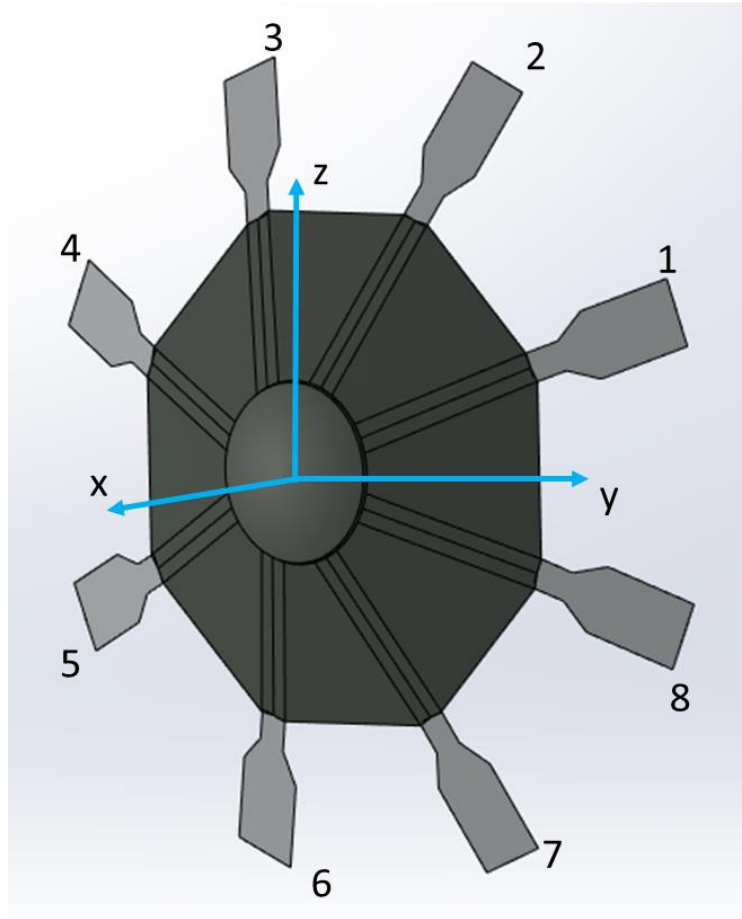


Figure 7 – Coordinate system definition

Table 3 – Flap number to rotation axis mapping

| Rotation Axis | Flap Numbers |
|---------------|--------------|
| Pitch         | 2,3,6,7      |
| Yaw           | 1,4,5,8      |

The control surface polarity definition is shown in Figure 8. A positive deflection is defined as deflecting into the airflow, and a negative deflection is defined as deflecting out of the airflow.

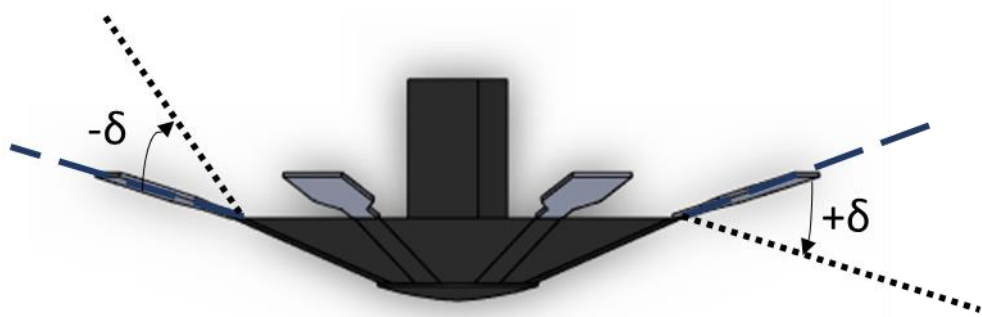


Figure 8 – Control surface polarity

## 2.2 Aerodynamic Analysis

The CFD analysis software, ANSYS Fluent, is utilized for the analysis of the aerodynamics of the system. To model the system dynamics effectively, a database of force and moment coefficients for a set of independent variables is necessary. These variables include: angle of attack ( $\alpha$ ), sideslip angle ( $\beta$ ), and flap deflection angle ( $\delta$ ). The conditions tested for these variables are shown in Table 4. A CFD simulation is executed for each permutation of the independent variables to obtain force and moment coefficients for each case. According to reference [3], these coefficients are independent of Mach number except in cases with relatively low Mach number ( $< 5$ ). Thus, a constant Mach number of 10 was used for all cases. By interpolation of the resulting database, the force and moment coefficients for any combination of the independent variables tested can be approximated.

Table 4 – Aerodynamic analysis variable conditions

| Variable       | Values Tested       |
|----------------|---------------------|
| $\alpha$ (deg) | -20, -10, 0, 10, 20 |
| $\beta$ (deg)  | -20, -10, 0, 10, 20 |
| $\delta$ (deg) | -20, -10, 0, 10, 20 |

The force and moment coefficients are related to the forces and moments acting on the vehicle through equations 2.1 and 2.2 respectively. These equations can be used to convert between the two sets of values. The density can be interpolated from the standard atmosphere table. The reference area and reference length are both properties of the structure. The reference area utilized is the taken to be the front-facing area of the structure, which is  $0.385 \text{ m}^2$  for the vehicle and  $0.026 \text{ m}^2$  per flap. The reference length for the vehicle is taken to be the diameter of the front of the vehicle, which is equal  $0.69 \text{ m}$ . For the flaps the distance to the centroid of the flap is added which results in  $0.84 \text{ m}$ . Note that all moments are taken with respect to the vehicle center of mass shown in Table 1.

$$C_F = \frac{2F}{\rho u^2 A} \quad (2.1)$$

$$C_M = \frac{2M}{\rho u^2 A(R)} \quad (2.2)$$

Where  $F$  is the force in Newtons,  $M$  is the moment in Nm,  $\rho$  is the density in  $\text{kg/m}^3$ ,  $u$  is the free-stream velocity in m/s,  $A$  is the Reference area in  $\text{m}^2$ , and  $R$  is the reference length in meters.

The initial setup for the CFD analysis is shown in Figure 9 below. To simplify the computations and reduce the number of permutations required, each flap was analyzed separately from the main vehicle structure. Figure 9 displays the configuration with all input variables equal to zero for both the ADEPT structure and Flap 1. The structures are placed inside an enclosure of four boundaries that define the control volume to be analyzed. The front boundary is defined as an inlet with velocity equivalent to Mach 10, and the back boundary is defined as an outlet. The remaining four boundaries are defined as walls with a specified shear stress of zero Pascals.

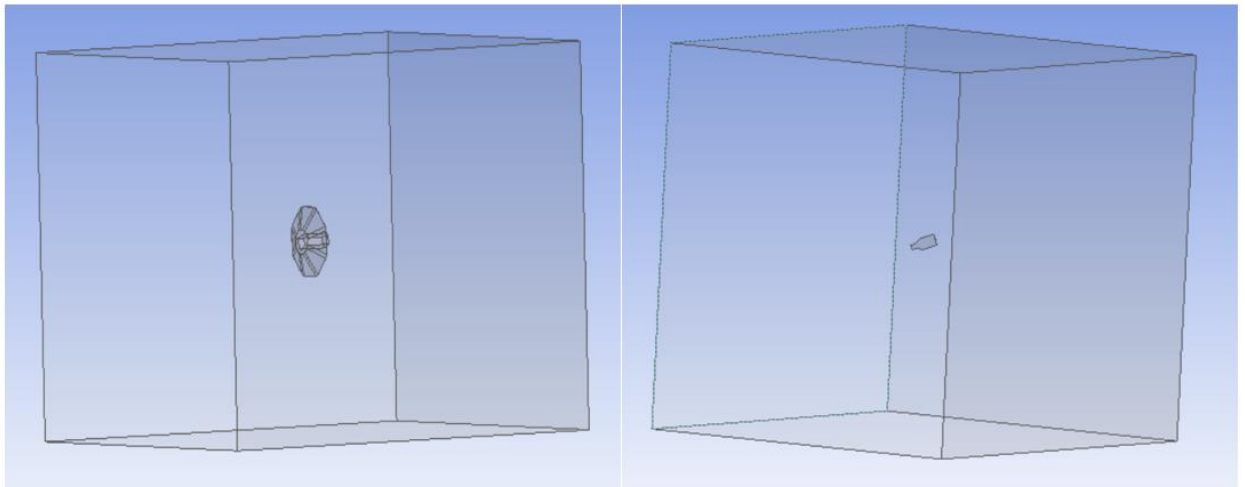


Figure 9 – ANSYS simulation initial setup

### 2.2.1 Mesh Analysis

To determine a suitable mesh for the calculations, a mesh sizing analysis was conducted. The objective of this analysis was to determine a mesh sizing that would provide an answer that is sufficiently accurate, while balancing the amount of computation power required to run the simulation. This was accomplished by starting out with a coarse mesh and incrementally increasing the fineness of the mesh. Iterations are continued until the effects on the final answer from further increments become negligible. The iterations were performed using the vehicle setup shown in Figure 9, with angle of attack and sideslip angle equal to zero. For each iteration the mesh element size was varied as a parameter, which results in a different number of mesh elements for each case.

The vehicle drag coefficient was used as the monitor to evaluate mesh performance. Results of this are shown in Figure 10. The top of the figure plots the computed drag coefficient versus the number of mesh elements for each case analyzed. The bottom plot shows the percent difference from the previous case. In cases with a number of elements below 200,000, there is shown to be large variations between iterations. As the number of elements increases beyond this value, the percent difference between the iterations trends toward zero, meaning the computation is converging on the correct solution. Additional iterations with increased element numbers

could be computed, but the accuracy benefits would be marginal when compared to the additional computation time that would be required. Thus, case 8 with 265,800 elements was selected. This case corresponds to an element size of 0.07 m. The resulting drag coefficient computed from this mesh is 1.451, which is comparable with the ADEPT vehicle drag coefficient plots shown in reference [3]. This provides further confidence in the CFD setup and the chosen mesh element size.

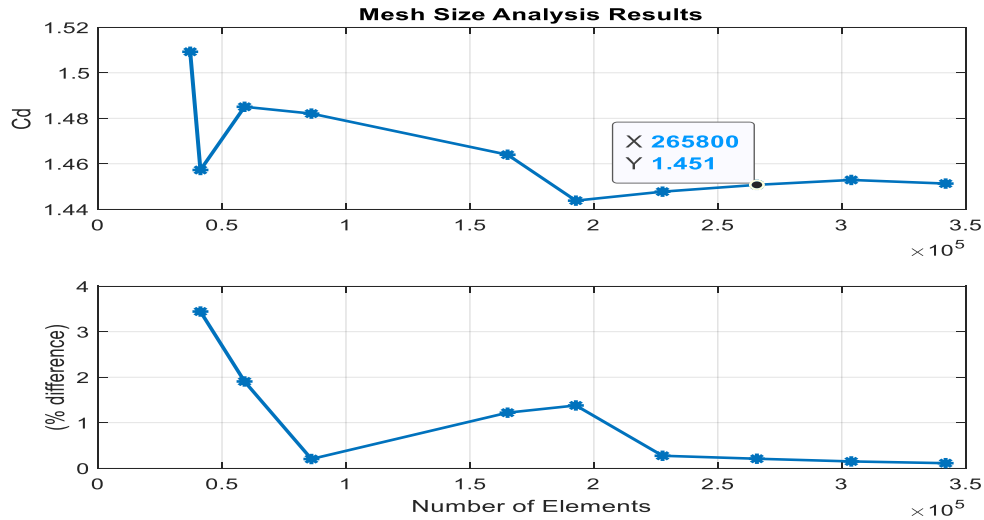


Figure 10 – Mesh sizing results

## 2.2.2 Results

After completion of the initial problem setup and meshing, the calculations were executed for each permutation of the variables presented in Table 4. Example results for the case consisting of the ADEPT vehicle with zero angle of attack and sideslip angle are shown in the following figures. Figure 11 and Figure 12 present the computation residuals and computed drag coefficients throughout the each iteration of the case. The two plots depict how the simulation converges on the solution as the iterations continue. The resulting velocity streamlines from the simulation are shown in Figure 13. The streamlines provide a visual confirmation that the calculations are being executed successfully.

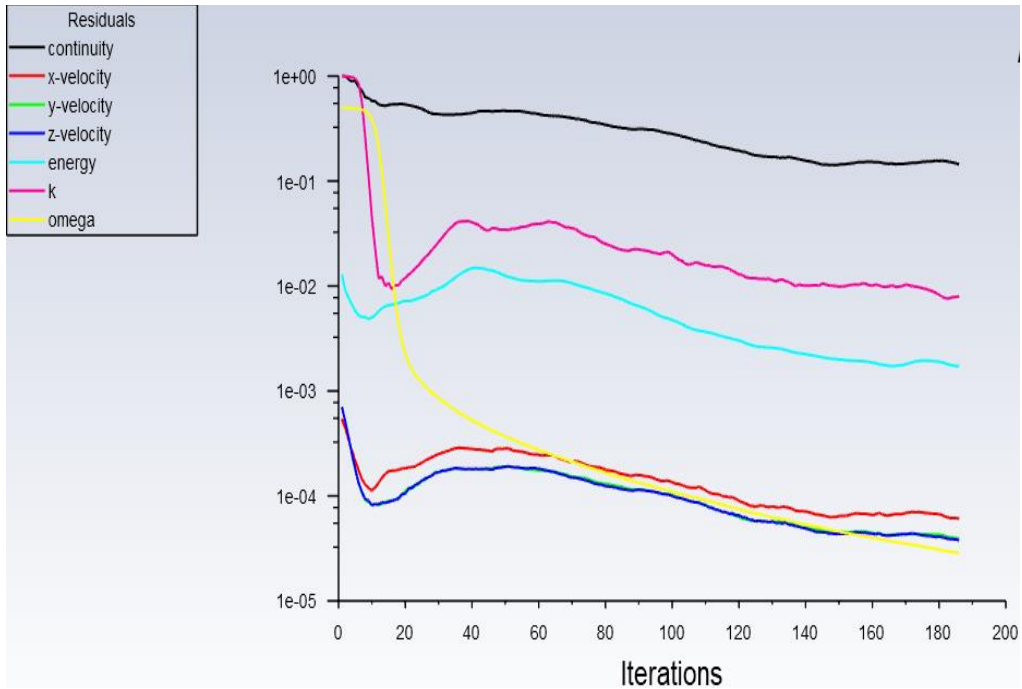


Figure 11 – Simulation scaled residuals

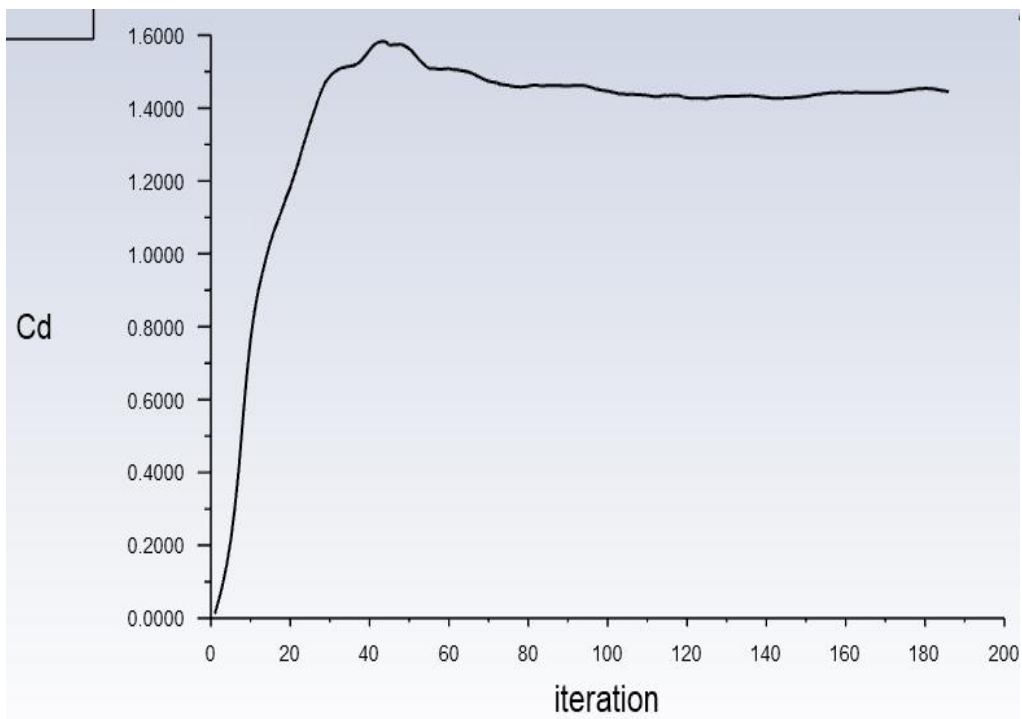


Figure 12 – Simulation drag coefficient

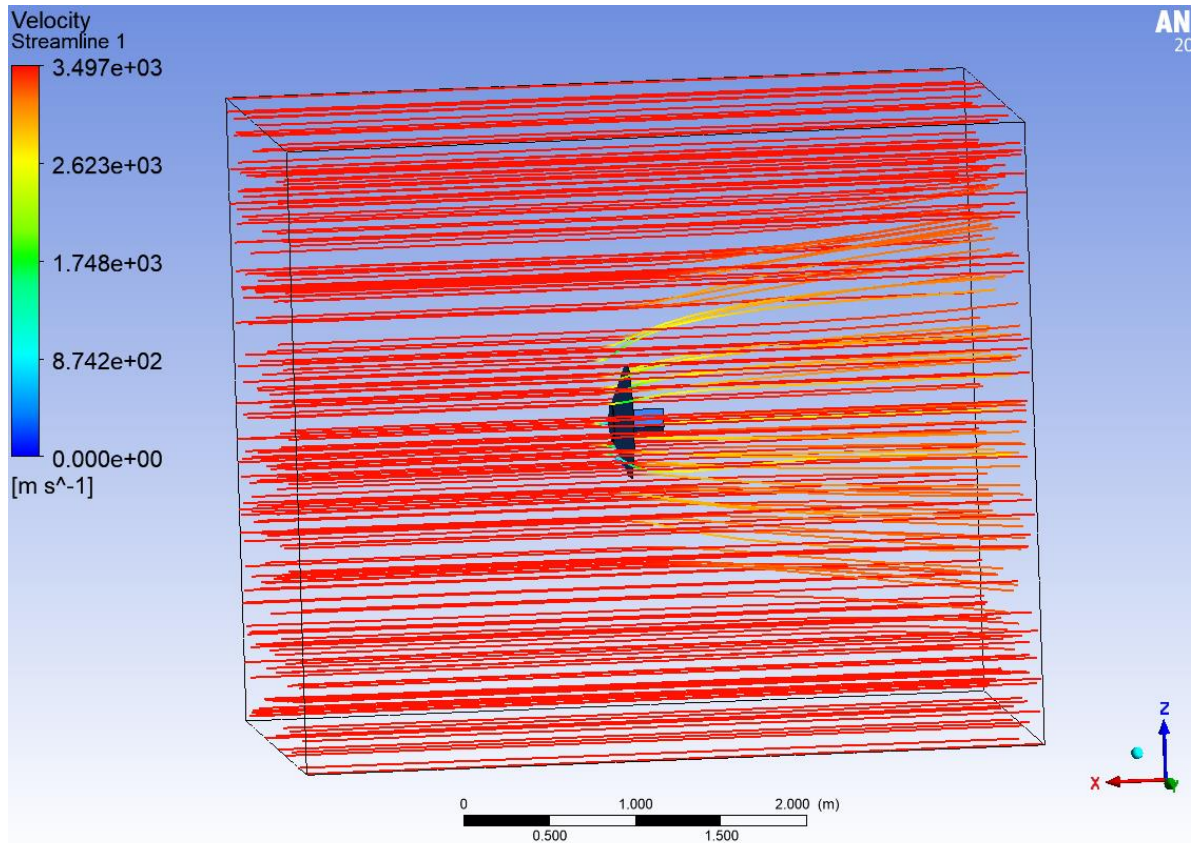


Figure 13 – CFD simulation streamline results

The results for the computed coefficients for the vehicle structure are shown in Figure 14. The aerodynamic force and moment coefficients are shown to be functions of angle of attack and sideslip angle. Similarly, the computations were repeated for each flap at the flap deflection angles listed in Table 4. The resulting data for the aerodynamic coefficients of flap one at zero angle of attack and sideslip are shown in Figure 15 to provide an example of the results.

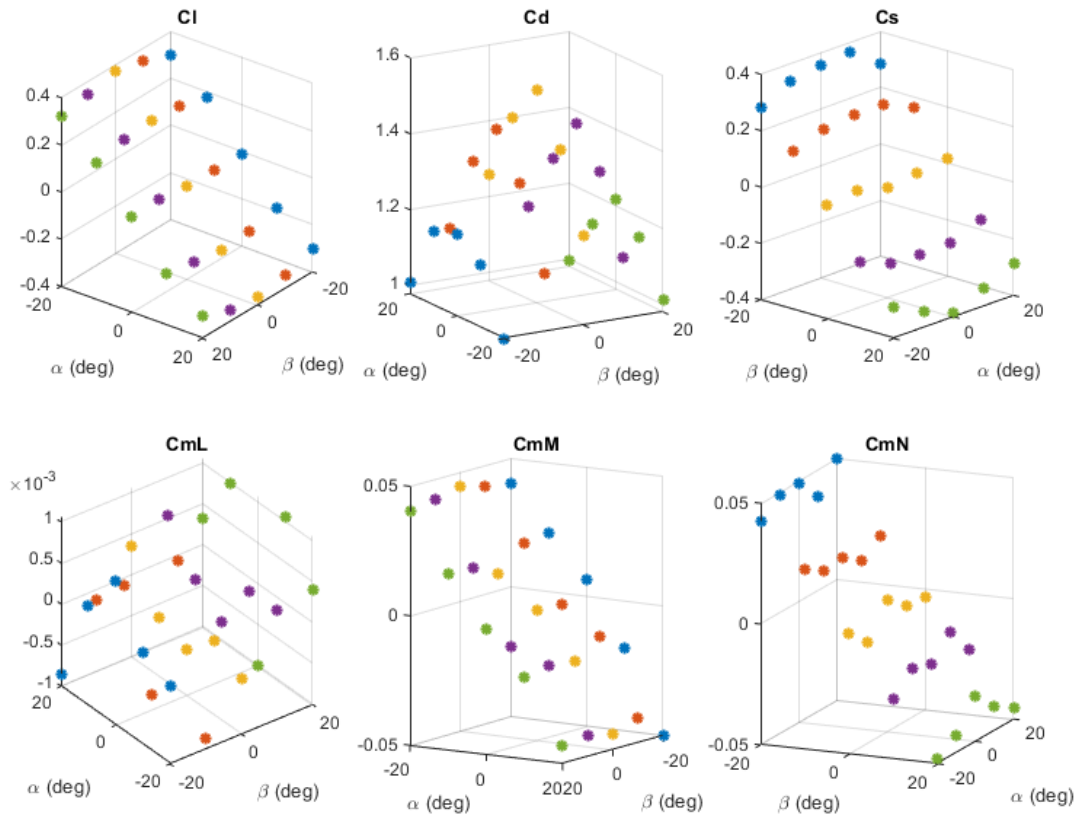


Figure 14 – ADEPT vehicle aerodynamic coefficients

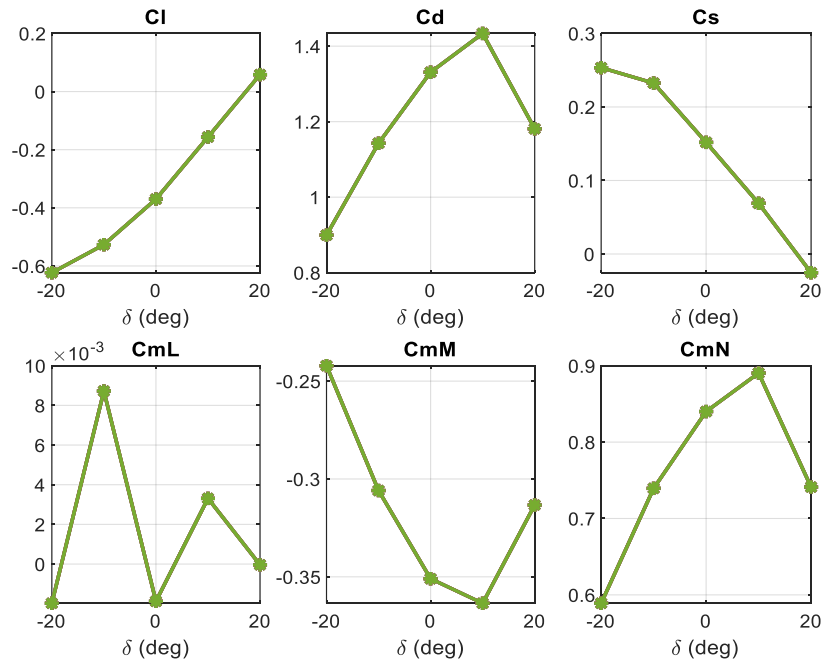


Figure 15 – Flap one aerodynamic coefficients (zero angle of attack and sideslip)



The CFD computations result in a database that can be queried to compute the forces and moments acting on the vehicle and each flap individually. The combined forces and moments can then be computed by summing these values, as shown below:

$$\vec{F}_{total} = \vec{F}_{ADEPT} + \sum_{n=1}^8 \vec{F}_{flap\_n} \quad (2.3)$$

$$\vec{M}_{total} = \vec{M}_{ADEPT} + \sum_{n=1}^8 \vec{M}_{flap\_n} \quad (2.4)$$

This concludes the description of the aerodynamic analysis performed on the system. The analysis generated aerodynamic force and moment coefficients to be utilized in further system modeling. This modeling is necessary to validate the performance of the aerodynamic flap control system to be discussed in later sections.

## 2.3 System Dynamics

This section summarizes the kinematic and dynamic equations used to model a hypersonic entry vehicle. These equations are described in reference [1] and provide a six degree of freedom representation of the system dynamics. First, the linear dynamics are described using equations 2.5 – 2.7.

$$\dot{V} = -\frac{g(z)}{m} \sin(\gamma) - \frac{1}{m} D \quad (2.5)$$

$$\dot{\gamma} = \left( -\frac{g(z)}{mV} + \frac{V}{z} \right) \cos(\gamma) + \frac{1}{mV} (L \cos(\sigma) - S \sin(\sigma)) \quad (2.6)$$

$$\dot{\xi} = \frac{1}{mV \cos(\gamma)} (L \sin(\sigma) + S \cos(\sigma)) \quad (2.7)$$

Where V is the velocity of the vehicle in m/s,  $\gamma$  is the flight path angle in radians,  $\xi$  is the heading angle in radians, L is the lift force, D is the drag force, S is the side force,  $g(z)$  is the force due to gravity (all forces in Newtons), z is the distance from the vehicle to Earth's center, and m is the mass of the vehicle.

Following this, the relationship describing the rotational dynamics of the system is presented in equation 2.8. Together with equations 2.5 – 2.7, the six degree dynamics of the system can be determined to propagate the states of the system in time.

$$\begin{bmatrix} \dot{p} \\ \dot{q} \\ \dot{r} \end{bmatrix} = I^{-1} \left( \begin{bmatrix} \mathcal{L} \\ \mathcal{M} \\ \mathfrak{N} \end{bmatrix} - \begin{bmatrix} p \\ q \\ r \end{bmatrix} \times I \begin{bmatrix} p \\ q \\ r \end{bmatrix} \right) \quad (2.8)$$

Where p, q, and r are the vehicle angular velocities in rad/s about the body x, y, and z axes respectively,  $\mathcal{L}$ ,  $\mathcal{M}$ , and  $\mathfrak{N}$  are the aerodynamic moments in Nm about roll, pitch, and yaw respectively, and I is the vehicle moment of inertia matrix in kg\*m<sup>2</sup>.

Lastly, the kinematic equations are provided in equations 2.9 – 3.4. Equations 2.9 – 2.11 describe the linear kinematics while equations 2.12 – 2.14 describe the rotational kinematics. These equations are utilized to compute the motion of the vehicle after the dynamic states have been updated.

$$\dot{z} = V \sin(\gamma) \quad (2.9)$$

$$\dot{\phi} = \frac{V}{z} \cos(\gamma) \cos(\xi) \quad (2.10)$$

$$\dot{\lambda} = \frac{V}{z \cos(\phi)} \cos(\gamma) \sin(\xi) \quad (2.11)$$

$$\dot{\sigma} = p \cos(\alpha) \sec(\beta) + r \sin(\alpha) \sec(\beta) \quad (2.12)$$

$$\dot{\alpha} = -p \cos(\alpha) \tan(\beta) + q - r \sin(\alpha) \tan(\beta) \quad (2.13)$$

$$\dot{\beta} = p \sin(\alpha) - r \cos(\alpha) \quad (2.14)$$

Where  $\phi$  is vehicle latitude and  $\lambda$  is vehicle longitude with both quantities measured in radians.

Figure 16 presents how the quantities from the aforementioned equations are defined with respect to the coordinate frame. The information and images provided in reference [1] were utilized to construct these images. The left side of the figure depicts the vehicle in an Earth Centered Earth Fixed (ECEF) reference frame. This image depicts how flight path angle and heading angle are defined with respect to the ECEF frame. The image on the right depicts how the angular displacements and body frame rotations are defined with respect to the vehicle path of motion.

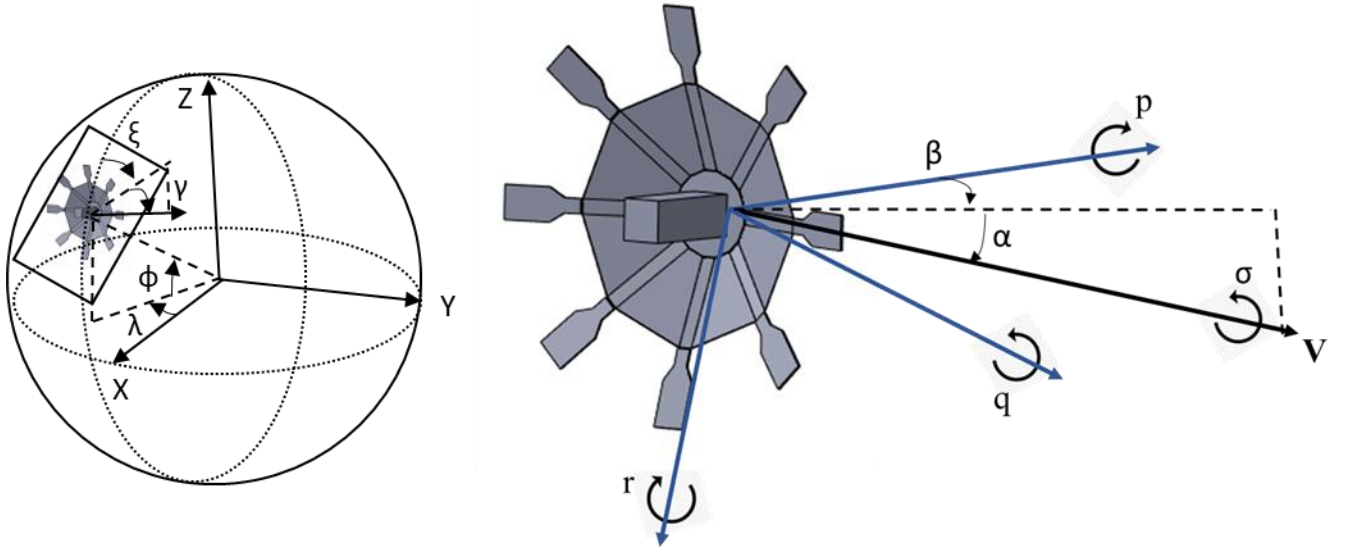


Figure 16 – Entry vehicle coordinate frames and vector definition

### 3 Control System Design

#### 3.1 Control System Architecture

Figure 17 depicts a block diagram of the control system. The entire control law is executed with a sampling rate of 500 Hz. The control system consists of the guidance law, the angle and rate controller, and the flap control allocation algorithm. The guidance law controls the flight path angle and heading angle of the vehicle velocity vector by generating angle of attack and sideslip angle commands. These commands are fed into the angle and rate controller which generate the angular acceleration commands necessary to produce the desired motion. Lastly, the acceleration commands are converted into flap deflection angles via the control allocation algorithm.

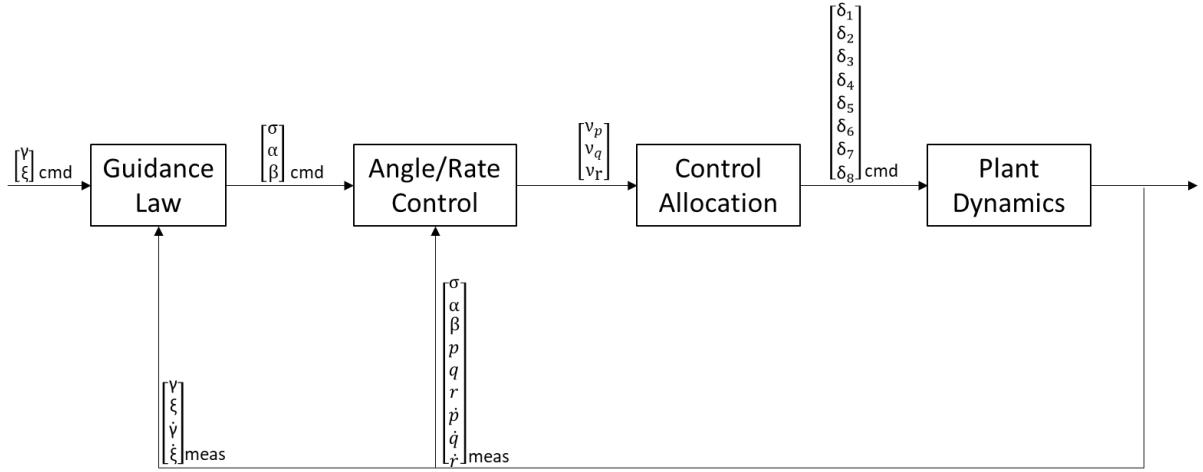


Figure 17 – Control system block diagram

#### 3.2 Dynamic Inversion Methodology

The guidance law and the angular rate controller both utilize the dynamic inversion process to generate control inputs. This section provides an overview of the dynamic inversion process. The dynamic inversion methodology discussed herein was formulated in reference [13]. Equation 3.1 represents the dynamic model of an arbitrary system. In this formulation,  $f(x,p)$  represents the system dynamics absent of any control inputs and  $G(x,p)$ , also known as the effector blending model, represents the contribution due to the control inputs. Additionally,  $x$  is the state vector,  $p$  is the parameter vector, and  $u$  is the control input vector.

$$\dot{x} = f(x,p) + G(x,p)u \quad (3.1)$$

The standard Nonlinear Dynamic Inversion (NDI) process serves as the basis for the approach. To begin this process, the state derivative in equation 3.1 is replaced by the virtual control input vector ( $v$ ). This implies that the virtual control input computed by the outer loop should be equal to the required state derivative. The system states ( $x$ ) and parameters ( $p$ ) are then replaced by the measured states ( $\hat{x}$ ) and measured parameters ( $\hat{p}$ ) respectively. After making these substitutions, equation 3.1 can be solved for the required control input which results in equation 3.2. This results in a formulation for the control law that relies heavily on the system dynamic model ( $f$ ). Thus, any model inaccuracies result in degradation of control system

performance. The INDI approach to be discussed reduces the reliance on system modeling by eliminating the need for a system dynamics model.

$$u = G(\hat{x}, \hat{p})^{-1}[v - f(\hat{x}, \hat{p})] \quad (3.2)$$

The INDI approach functions by computing an incremental input  $\Delta u$  with respect to the states of the system from the previous timestep. To formulate the incremental input, equation 3.1 is approximated using a first order Taylor series expansion (3.3). It is assumed that the changes in the states occur significantly slower than the changes in the control input, thus equation 3.3 can be reduced to equation 3.4. To ensure that this assumption is valid, the control system sample rate must be selected such that it is significantly faster than the state dynamics. Note that  $x_0$  and  $u_0$  refer to the states and control inputs at the previous timestep.

$$\dot{x} \approx \dot{x}_0 + \frac{\partial}{\partial x} [f(x, p) + G(x, p)u] \big|_{x=x_0, u=u_0} \Delta x + \frac{\partial}{\partial u} [f(x, p) + G(x, p)u] \big|_{x=x_0, u=u_0} \Delta u \quad (3.3)$$

$$\dot{x} \approx \dot{x}_0 + G(x_0, p) \Delta u \quad (3.4)$$

The virtual control input,  $v$ , is substituted for the state derivative in equation 3.4 and the equation is rearranged to solve for the incremental control input. The final formulation for the incremental control input is shown by equation 3.5. The computed incremental input is added to the summed input from the previous sample to update the total input, as shown by equation 3.6.

$$\Delta u \approx G^{-1}(\hat{x}_0, \hat{p})(v - \dot{\hat{x}}_0) \quad (3.5)$$

$$u = \hat{u}_0 + \Delta u \quad (3.6)$$

The advantage of utilizing this formulation is that the only modeling information required is the effector blending model. Meaning that it is only required to know the effect of the control inputs on the dynamics, rather than relying on a full dynamics model of the vehicle. This reduces the effects of modeling errors on control system performance by relying on the state feedback instead.

### 3.3 Guidance Law

The guidance law architecture is depicted by Figure 18 below. The algorithm subtracts the measured flight path and heading angles from the commanded values to generate an error signal. The error signal is fed through a proportional-integral (PI) controller to generate the virtual control inputs  $v_\gamma$  and  $v_\xi$ . The model inversion block implements either the NDI or INDI inversion and the outputs are combined with the virtual control inputs to determine the desired lift and side forces. After the lift and side forces have been computed, the angle allocation algorithm translates these into the required vehicle angle of attack and sideslip angle. These commands go through a saturator which limits the commanded angles between plus or minus 15 degrees. The angle limiter also includes anti-windup logic to zero the error integrator when the control signal has been saturated.

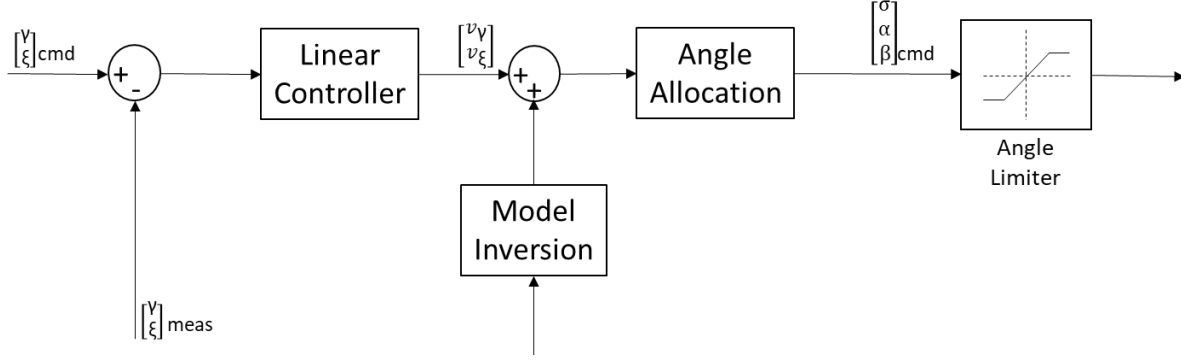


Figure 18 – Guidance law block diagram

The gains for the PID controller are tabulated in Table 5 below where  $k_{pg}$  and  $k_{ig}$  are the guidance proportional and integral gains respectively. Note that the same gain set is used for both flight path angle and heading angle.

Table 5 – Guidance control law gains

| Identifier | Value |
|------------|-------|
| $k_{pg}$   | 1.92  |
| $k_{ig}$   | 0.40  |

### 3.3.1 Dynamic Inversion

#### 3.3.1.1 Nonlinear Dynamic Inversion

This subsection discusses the dynamic inversion of the translational states of the system using the NDI approach. Equation 2.6 can be written in terms of the required flight path angle state derivative as shown by equation 3.7.

$$\dot{\gamma}_{req} = \left( -\frac{g(z)}{mV} + \frac{V}{z} \right) \cos(\gamma) + \frac{1}{mV} (L \cos(\sigma) - S \sin(\sigma)) \quad (3.7)$$

The total lift force and side force is then split into the lift provided by the vehicle ( $L_v$ ,  $S_v$ ) and the lift provided by the control surfaces ( $L_{cs}$ ,  $S_{cs}$ ) to obtain equation 3.8.

$$\begin{aligned} \dot{\gamma}_{req} = \left( -\frac{g(z)}{mV} + \frac{V}{z} \right) \cos(\gamma) + \frac{1}{mV} (L_v \cos(\sigma) - S_v \sin(\sigma)) \\ + \frac{1}{mV} (L_{cs} \cos(\sigma) - S_{cs} \sin(\sigma)) \end{aligned} \quad (3.8)$$

The guidance law controls the vehicle flight path angle and heading angle by adjusting the vehicle angle of attack and sideslip angle to generate the necessary lift and side forces. Thus, the objective is to solve equation 3.8 for the vehicle lift and side forces. This results in equation 3.9.

$$\begin{bmatrix} \cos(\sigma) & -\sin(\sigma) \end{bmatrix} \begin{bmatrix} L_v \\ S_v \end{bmatrix} = mV \dot{\gamma}_{req} + \left( g(z) - \frac{mV^2}{z} \right) \cos(\gamma) - L_{cs} \cos(\sigma) + S_{cs} \sin(\sigma) \quad (3.9)$$

The same process is followed for the vehicle heading angle. Equation 3.10 presents the required heading state derivative with the lift and side forces split between the vehicle and the control surface contributions.

$$\dot{\xi}_{req} = \frac{1}{mV\cos(\gamma)}(L_V\sin(\sigma) + S_V\cos(\sigma)) + \frac{1}{mV\cos(\gamma)}(L_{CS}\sin(\sigma) + S_{CS}\cos(\sigma)) \quad (3.10)$$

Equation 3.10 is rewritten to solve for the vehicle lift and side force as shown by equation 3.11.

$$\begin{bmatrix} \sin(\sigma) & \cos(\sigma) \end{bmatrix} \begin{bmatrix} L_V \\ S_V \end{bmatrix} = mV\cos(\gamma)\dot{\xi}_{req} - L_{CS}\sin(\sigma) - S_{CS}\cos(\sigma) \quad (3.11)$$

Equation 3.9 and 3.11 form a system of equations with two equations and two unknowns. Equation 3.12 represents this system in matrix form, with the bank angle rotation matrix ( $B_{rot}$ ) defined in equation 3.13.

$$B_{rot} \begin{bmatrix} L_V \\ S_V \end{bmatrix} = \begin{bmatrix} mV\dot{\gamma}_{req} + \left(g(z) - \frac{mV^2}{z}\right)\cos(\gamma) - L_{CS}\cos(\sigma) + S_{CS}\sin(\sigma) \\ mV\cos(\gamma)\dot{\xi}_{req} - L_{CS}\sin(\sigma) - S_{CS}\cos(\sigma) \end{bmatrix} \quad (3.12)$$

$$B_{rot} = \begin{bmatrix} \cos(\sigma) & -\sin(\sigma) \\ \sin(\sigma) & \cos(\sigma) \end{bmatrix} \quad (3.13)$$

Both sides of 3.12 are matrix multiplied by the inverse of the bank angle rotation matrix to solve for the lift and side forces explicitly (3.14).

$$\begin{bmatrix} L_V \\ S_V \end{bmatrix} = B_{rot}^{-1} \begin{bmatrix} mV\dot{\gamma}_{req} + \left(g(z) - \frac{mV^2}{z}\right)\cos(\gamma) - L_{CS}\cos(\sigma) + S_{CS}\sin(\sigma) \\ mV\cos(\gamma)\dot{\xi}_{req} - L_{CS}\sin(\sigma) - S_{CS}\cos(\sigma) \end{bmatrix} \quad (3.14)$$

### 3.3.1.2 Incremental Nonlinear Dynamic Inversion

Next, the incremental commands for INDI processing are determined. Following the process outlined in section 3.2, equation 3.8 is linearized using a first order Taylor approximation which results in equation 3.15.

$$\begin{aligned} & \dot{\gamma}_{req} = \dot{\gamma}_0 \\ & + \frac{\partial}{\partial \gamma} \left[ \left( -\frac{g(z)}{mV} + \frac{V}{z} \right) \cos(\gamma) + \frac{1}{mV} ((L_V + L_{CS})\cos(\sigma) - (S_V + S_{CS})\sin(\sigma)) \right] \Big|_{\gamma, \sigma, L, S = \gamma_0, \sigma_0, L, S} \Delta \gamma \\ & + \frac{\partial}{\partial \sigma} \left[ \left( -\frac{g(z)}{mV} + \frac{V}{z} \right) \cos(\gamma) + \frac{1}{mV} ((L_V + L_{CS})\cos(\sigma) - (S_V + S_{CS})\sin(\sigma)) \right] \Big|_{\gamma, \sigma, L, S = \gamma_0, \sigma_0, L, S} \Delta \sigma \\ & + \frac{\partial}{\partial L} \left[ \left( -\frac{g(z)}{mV} + \frac{V}{z} \right) \cos(\gamma) + \frac{1}{mV} ((L_V + L_{CS})\cos(\sigma) - (S_V + S_{CS})\sin(\sigma)) \right] \Big|_{\gamma, \sigma, L, S = \gamma_0, \sigma_0, L, S} \Delta L \\ & + \frac{\partial}{\partial S} \left[ \left( -\frac{g(z)}{mV} + \frac{V}{z} \right) \cos(\gamma) + \frac{1}{mV} ((L_V + L_{CS})\cos(\sigma) - (S_V + S_{CS})\sin(\sigma)) \right] \Big|_{\gamma, \sigma, L, S = \gamma_0, \sigma_0, L, S} \Delta S \end{aligned} \quad (3.15)$$

By applying the time-scale separation assumption and making use of the knowledge that the forces generated by the flaps is negligible compared to the vehicle forces, equation 3.15 reduces into equation 3.16. Equation 3.16 is then rearranged to solve for  $\Delta L_V$  and  $\Delta S_V$  to obtain equation 3.17. Equation 3.17 represents the incremental lift and side forces needed to be provided by the vehicle to control the vehicle flight path angle.

$$\dot{\gamma}_{req} = \dot{\gamma}_0 + \frac{1}{mV} (\Delta L_V \cos(\sigma) - \Delta S_V \sin(\sigma)) \quad (3.16)$$

$$\begin{bmatrix} \cos(\sigma) & \sin(\sigma) \end{bmatrix} \begin{bmatrix} \Delta L_V \\ \Delta S_V \end{bmatrix} = mV (\dot{\gamma}_{req} - \dot{\gamma}_0) \quad (3.17)$$

The same process is followed for the vehicle heading angle. Equation 3.10 is linearized using a first order Taylor approximation and simplified using the time-scale separation assumption. This results in equation 3.18, which is then rearranged to solve for the incremental side force which is shown by equation 3.19.

$$\dot{\xi}_{req} = \dot{\xi}_0 + \frac{1}{mV \cos(\gamma)} (\Delta L_V \sin(\sigma) + \Delta S_V \cos(\sigma)) \quad (3.18)$$

$$\begin{bmatrix} \sin(\sigma) & \cos(\sigma) \end{bmatrix} \begin{bmatrix} \Delta L_V \\ \Delta S_V \end{bmatrix} = mV \cos(\gamma) (\dot{\xi}_{req} - \dot{\xi}_0) \quad (3.19)$$

Equations 3.17 and 3.19 are then combined into a matrix equation and manipulated to compute the total incremental lift and side forces required. This is represented by equation 3.20 below.

$$\begin{bmatrix} \Delta L_V \\ \Delta S_V \end{bmatrix} = B_{rot}^{-1} \begin{bmatrix} mV (\dot{\gamma}_{req} - \dot{\gamma}_0) \\ mV \cos(\gamma) (\dot{\xi}_{req} - \dot{\xi}_0) \end{bmatrix} \quad (3.20)$$

The implementation of the INDI approach requires filtering on the commands and state derivatives. This is done to attenuate the noise caused by differentiation in the control law, as well as noise on the state feedback measurements. A first-order Butterworth filter with a cutoff frequency of 250 Hz is implemented. The filter is represented by the discrete time transfer function below (3.21) and the corresponding filter coefficients are tabulated in Table 6.

$$F(z) = \frac{Az+B}{Cz+D} \quad (3.21)$$

Table 6 – Discrete filter coefficients

| Identifier | Value<br>(dimensionless) |
|------------|--------------------------|
| A          | 0.5                      |
| B          | 0.5                      |
| C          | 1                        |
| D          | -5.51e-17                |

The discretized filter is implemented using the following difference equation:

$$y(n) = \frac{Ax(n) + Bx(n-1) - Dy(n-1)}{c} \quad (3.22)$$

Where  $x$  represents the filter inputs,  $y$  represents the outputs, and  $n$  represents the current sample. The frequency response plot of the filter is shown in Figure 19.

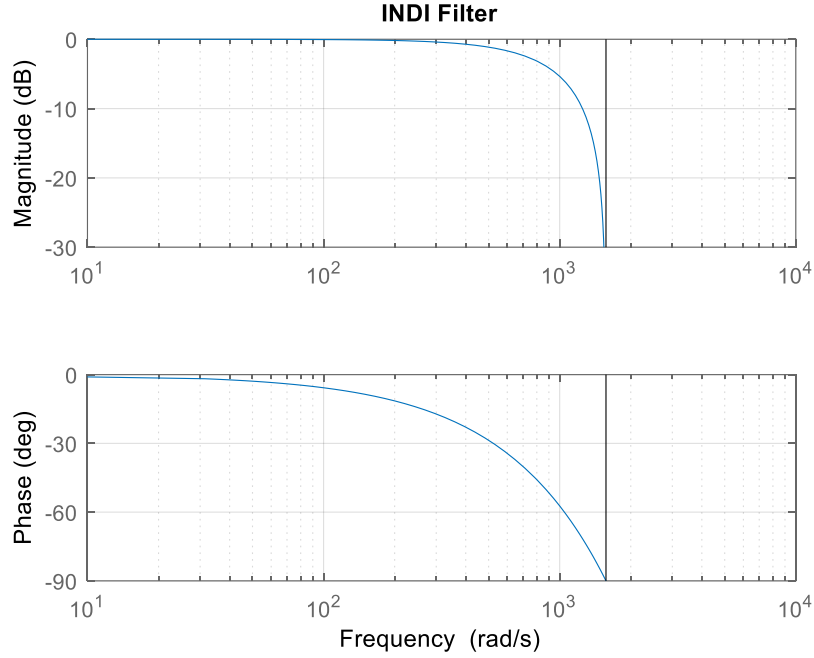


Figure 19 – INDI filter frequency response

### 3.3.2 Angle Allocation

The lift and side forces computed by the dynamic inversion process are used to calculate the angle of attack and sideslip angle commands. A linear fit of the CFD data is used to determine the vehicle lift as a function of angle of attack, and side force as a function of sideslip angle for a given set of flight conditions. The required angle of attack and sideslip are then computed using the slope and intercept of this linear fit. The bank angle command is set equal to zero throughout flight as it is not needed to control the vehicle trajectory.

### 3.4 Angle and Rate Controller

The angle control module of the control law consists of two feedback control loops in series. The outermost loop implements a proportional controller on the error between the commanded and measured angular displacements. This loop outputs roll, pitch and yaw rate commands that are fed through saturation logic that limits the command rates within plus or minus 10 deg/sec. The limited rate commands are fed into the inner angular rate control loop. The rate controller implements a proportional control law on the rate error to generate angular acceleration commands. The acceleration commands are combined with the dynamic inversion inputs to determine the required roll, pitch and yaw moments which are output to the control allocation module.



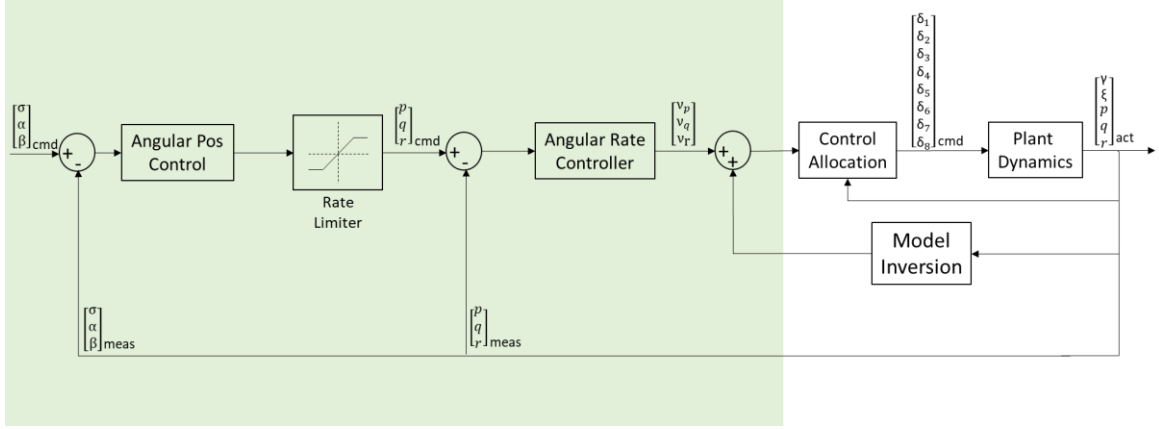


Figure 20 – Angle and rate controller block diagram

The control gains for the angle ( $k_{pa}$ ) and rate ( $k_{pr}$ ) proportional controllers are tabulated in Table 7. The same gains are used across all three control axes.

Table 7 – Angle and rate control gains

| Identifier | Value |
|------------|-------|
| $k_{pa}$   | 6.0   |
| $k_{pr}$   | 18.0  |

### 3.4.1 Coordinate Transformation

The angular position controller outputs the required bank, angle of attack and sideslip angular rates. These rates must be transformed into the body frame roll, pitch, and yaw rotation rates in order to be utilized by the angular rate controller. This transformation is computed by manipulating equations 2.12-2.14 to solve for the required body rates, resulting in the following equations:

$$p_{req} = \frac{\dot{\sigma}_{req} - r \sin(\alpha) \sec(\beta)}{\cos(\alpha) \sec(\beta)} \quad (3.23)$$

$$q_{req} = \dot{\alpha}_{req} + p \cos(\alpha) \tan(\beta) + r \sin(\alpha) \tan(\beta) \quad (3.24)$$

$$r_{req} = \frac{-\dot{\beta}_{req} + p \sin(\alpha)}{\cos(\alpha)} \quad (3.25)$$

### 3.4.2 Dynamic Inversion

#### 3.4.2.1 Nonlinear Dynamic Inversion

This section describes the dynamic inversion process for the vehicle rotational states. The original derivations for these equations are provided in reference [13]. Equation 2.8 can be rewritten in terms of the total aerodynamic moments. The total moment is then split into the individual contributions from the vehicle and control surfaces. Equation 3.26 represents this relationship.

$$M_{tot} = M_{CS} + M_V = I \dot{\omega}_{req} + \omega \times I \omega \quad (3.26)$$

Equation 3.26 is rearranged to solve for the required moment contribution from the control surfaces to control the vehicle rotational states. The resulting equation is expanded and shown by equations 3.27-3.29.

$$\mathcal{L}_{req} = \mathcal{L}_{CS} = I_{XX}\dot{p}_{req} - I_{XZ}r - q(I_{XZ}p - I_{ZZ}r) - I_{YY}qr - \mathcal{L}_V \quad (3.27)$$

$$\mathcal{M}_{req} = \mathcal{M}_{CS} = I_{YY}\dot{q}_{req} + r(I_{XX}q - I_{XZ}r) + p(I_{XZ}p - I_{ZZ}r) - \mathcal{M}_V \quad (3.28)$$

$$\mathfrak{N}_{req} = \mathfrak{N}_{CS} = I_{ZZ}\dot{r}_{req} - I_{XZ}\dot{p}_{req} - q(I_{XX}p - I_{XZ}r) + I_{YY}pq - \mathfrak{N}_V \quad (3.29)$$

### 3.4.2.2 Incremental Nonlinear Dynamic Inversion

To solve for the INDI control requirements, Equation 3.26 is rearranged to solve for the required angular velocity (3.30).

$$\dot{\omega}_{req} = \mathbf{I}^{-1}[\mathbf{M}_{CS} + \mathbf{M}_V - \omega \times \mathbf{I}\omega] \quad (3.30)$$

Equation 3.30 is then linearized using a first order Taylor expansion which results in equation 3.31.

$$\begin{aligned} \dot{\omega}_{req} = \dot{\omega}_0 + \frac{\partial}{\partial \omega} [\mathbf{I}^{-1}[\mathbf{M}_V - \omega \times \mathbf{I}\omega]]_{\omega, \mathbf{M}_{CS}=\omega_0, \mathbf{M}_{CS0}} \Delta\omega \\ + \frac{\partial}{\partial \mathbf{M}_{CS}} [\mathbf{I}^{-1}\mathbf{M}_{CS}]_{\omega, \mathbf{M}_{CS}=\omega_0, \mathbf{M}_{CS0}} \Delta\mathbf{M}_{CS} \end{aligned} \quad (3.31)$$

Equation 3.31 is simplified by applying the assumption that  $\Delta\omega \ll \Delta\mathbf{M}_{CS}$ , thus obtaining equation 3.32. This equation can be rearranged to solve for the incremental control surface moment requirement (3.33).

$$\dot{\omega}_{req} = \dot{\omega}_0 + \frac{\partial}{\partial \mathbf{M}_{CS}} [\mathbf{I}^{-1}\mathbf{M}_{CS}]_{\omega, \mathbf{M}_{CS}=\omega_0, \mathbf{M}_{CS0}} \Delta\mathbf{M}_{CS} \quad (3.32)$$

$$\Delta\mathbf{M}_{CS} = \mathbf{I}(\dot{\omega}_{req} - \dot{\omega}_0) \quad (3.33)$$

The rate control INDI algorithm implements the same filter described for the guidance law in section 3.3.1.2.

## 3.5 Control Allocation

After computing the required moments, the control law determines the corresponding allocation of the control inputs (control surface deflection angles). The control allocation is computed using the Weighted Least Squares (WLS) approach discussed in reference [13]. This approach formulates a quadratic cost function and then solves the resulting optimization problem. The optimization problem is solved using a WLS algorithm to compute the optimal control inputs. This is implemented in the control law to determine the necessary control surface deflections while balancing constraints on the control inputs and state variables. The cost function to be optimized is presented by equation 3.34 below.

$$\min \|W_u(u - u_d)\|^2 + \mu \|W_v(Bu - v)\|^2 \quad (3.34)$$

Where  $v$  is the virtual control input,  $u$  is the physical control input,  $u_d$  is the desired physical control input,  $B$  is the control effectiveness matrix,  $\mu$  is the relative weighting constant between the physical control inputs and virtual control inputs,  $W_u$  is the physical control weighting matrix and  $W_v$  is the virtual control weighting matrix.

The virtual control inputs are the products of the dynamic inversion process. For the NDI method, these inputs are  $[\mathcal{L}_{req} \mathcal{M}_{req} \mathfrak{N}_{req}]^T$ . For INDI, they are the incremental versions of these commands:  $[d\mathcal{L}_{req} d\mathcal{M}_{req} d\mathfrak{N}_{req}]^T$ . The physical control inputs are the flap deflection angles represented by  $[\delta_1 \delta_2 \delta_3 \delta_4 \delta_5 \delta_6 \delta_7 \delta_8]^T$ .

The control effectiveness matrix ( $B$ ) represents the control authority of each flap on the three virtual control inputs. The matrix consists of the localized slopes of the flap aerodynamic moment coefficients with respect to changes in deflection angle. The coefficients are multiplied by the dynamic pressure to obtain the scaled forces and moments. This is represented below:

$$B = \frac{1}{2}\rho V^2 \left( \frac{d}{d\delta} \begin{bmatrix} C_{L1} & C_{L2} & C_{L3} & C_{L4} & C_{L5} & C_{L6} & C_{L7} & C_{L8} \\ C_{M1} & C_{M2} & C_{M3} & C_{M4} & C_{M5} & C_{M6} & C_{M7} & C_{M8} \\ C_{N1} & C_{N2} & C_{N3} & C_{N4} & C_{N5} & C_{N6} & C_{N7} & C_{N8} \end{bmatrix} \right) \quad (3.35)$$

It is worth noting that a control surface deflection angle of zero does not correspond to zero aerodynamic moments. Thus, for NDI the zero deflection moment values must be subtracted from the virtual input as a bias term in order to calculate the deflection angles correctly. This step is not required for INDI since it is computing a relative command rather than an absolute one.

The control weighting matrices ( $W_u$  and  $W_v$ ) define the relative importance between their corresponding inputs. For the physical control inputs all flaps are weighted evenly, thus  $W_u$  is an 8x8 identity matrix. Similarly, the virtual control inputs are weighted evenly making  $W_v$  a 3x3 identity matrix. The relative weighting constant ( $\mu$ ) is set equal to  $10^{-6}$  to prioritize the weighting on the physical control inputs.

The control allocation law imposes limits on the calculated control surface inputs. These limits are set to prevent from commanding the control surfaces beyond their operational limits. There are limits imposed by the maximum deflection range of the flaps, as well as the maximum distance the flaps can deflect in a single control sample. The maximum flap deflection angle ( $\delta_{max}$ ) is equal to twenty degrees in the positive and negative directions. For NDI the upper and lower bounds of the command ( $u_{min}$  and  $u_{max}$ ) are simply set equal to minimum and maximum flap deflections. For INDI, the bounds on the incremental commands ( $du_{min}$  and  $du_{max}$ ) are computed by taking the difference between the absolute bounds and the current flap deflections. To determine the limits imposed by the maximum rates, the maximum deflection rate ( $\dot{\delta}_{max}$ ) is multiplied by the control system sample time ( $t_s$ ) to determine the maximum deflection over a given control sample. A deflection rate of 200 deg/sec is used as the maximum deflection rate. After both sets of limits have been calculated, the most constraining set is chosen as the allocation limits. The control allocation limits are summarized in Table 8.

Table 8 – Control allocation input bounds

| <b>NDI</b>  | Limit (deg)  |
|-------------|--|
| $u_{\min}$  | $\max(-\delta_{\max}, \delta - \dot{\delta}_{\max} \times t_s)$  |
| $u_{\max}$  | $\min(\delta_{\max}, \delta + \dot{\delta}_{\max} \times t_s)$   |
| <b>INDI</b> |  |
| $du_{\min}$ | $\max(-\delta_{\max} - \delta, -\dot{\delta}_{\max} \times t_s)$ |
| $du_{\max}$ | $\min(\delta_{\max} - \delta, \dot{\delta}_{\max} \times t_s)$   |

The desired control input ( $u_d$ ) enforces a constraint that forces the computed deflection angles to be as close as possible to a specified location. It is desired that the control surface deflections remain near zero for the duration of the flight. Thus, for NDI this parameter is simply set to zero for all flaps. For the incremental approach, this parameter is calculated by taking the difference between zero and the current deflection angle. In both cases, the resulting control inputs should trend towards zero whenever possible.

The aforementioned parameters and computations complete the setup of the quadratic cost function in the controller. The associated optimization problem is then solved using an active set method [13]. An active set algorithm from a MATLAB toolbox obtained from reference [14] is utilized to compute the solution. The outputs of this solution are the optimized flap deflections that provide the necessary aerodynamic moments.

## 4 Simulation Results

This section presents the simulation results for the hypersonic re-entry vehicle utilizing the flap control system. Each control loop is tested individually starting from the innermost loop and moving outward. Results are presented for both NDI and INDI inversion schemes and overlaid to compare performance. All results in sections 4.1.1 through 4.1.3 utilize the same initial flight conditions with an initial altitude of 100 km and a starting Mach number of 30.

### 4.1 Angle and Rate Controller

#### 4.1.1 Dynamic Inversion

Prior to testing the closed-loop rate control module, both dynamic inversion modules are tested open loop. To accomplish this, acceleration commands coming from the rate controller are replaced with constant acceleration inputs. This is done to verify that the performance of dynamic inversion and the control allocation is as expected. Theoretically if the dynamic inversion functions perfectly, the resulting rate output would be a simple integration of the commanded acceleration.

Figure 21 and Figure 22 below shows the results of testing the rate control NDI algorithm open-loop. A constant acceleration of  $1 \text{ m/sec}^2$  is commanded in both pitch and yaw while the roll acceleration is held at zero. The acceleration plots show that after an initial transient, the accelerations reach the commanded values and remain there for the remainder of the simulation. Additionally the rate plots look as expected with the pitch and yaw rates showing a ramp with a constant slope of  $1 \text{ deg/sec}^2$ . The roll axis is held constant with a small offset from zero caused by the initial transient. This offset is expected due to the fact that the dynamic inversion is running open-loop.

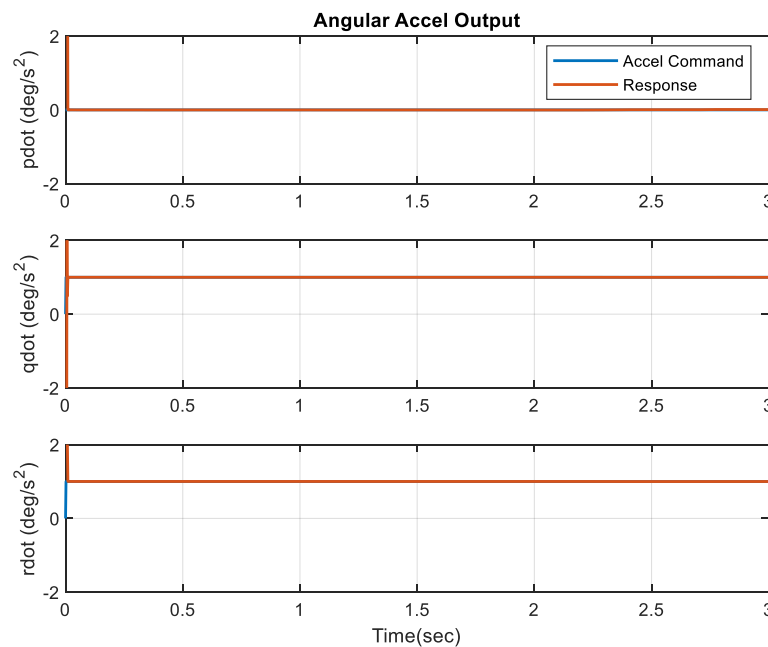


Figure 21 – NDI test acceleration output

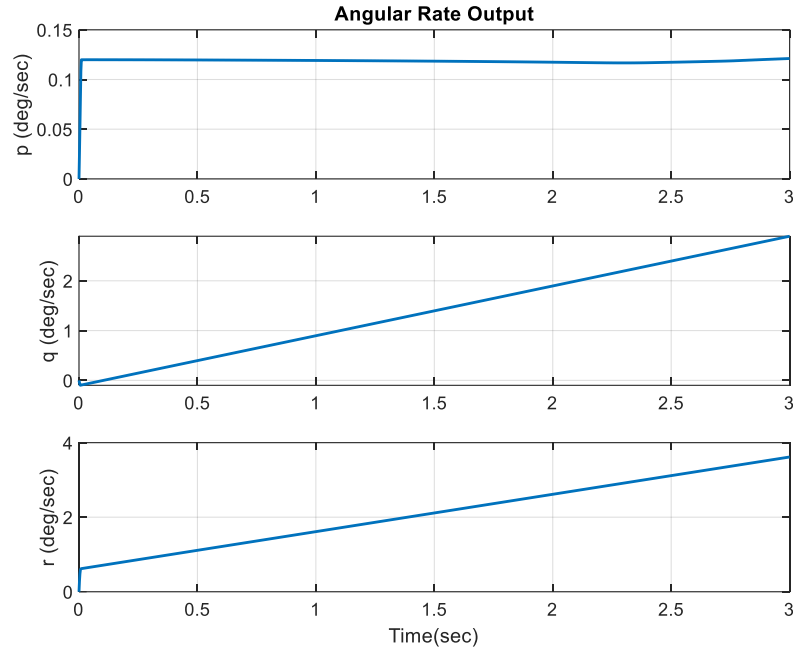


Figure 22 – NDI test rate output

The flap deflection angles for the NDI test are shown in Figure 23. The deflection angles are initialized to zero degrees and the control allocation algorithm successfully commands them to the positions necessary to respond to the dynamic inversion outputs. The torque requirements vary as the vehicle rates increase which results in the variation of the deflection angles throughout the test. It can also be observed that flap 5 saturates as the vehicle rates and rotation angles increase. Saturation of the control inputs can result in degradation of control system performance, which is why a rate limiter is implemented in the rate control loop.

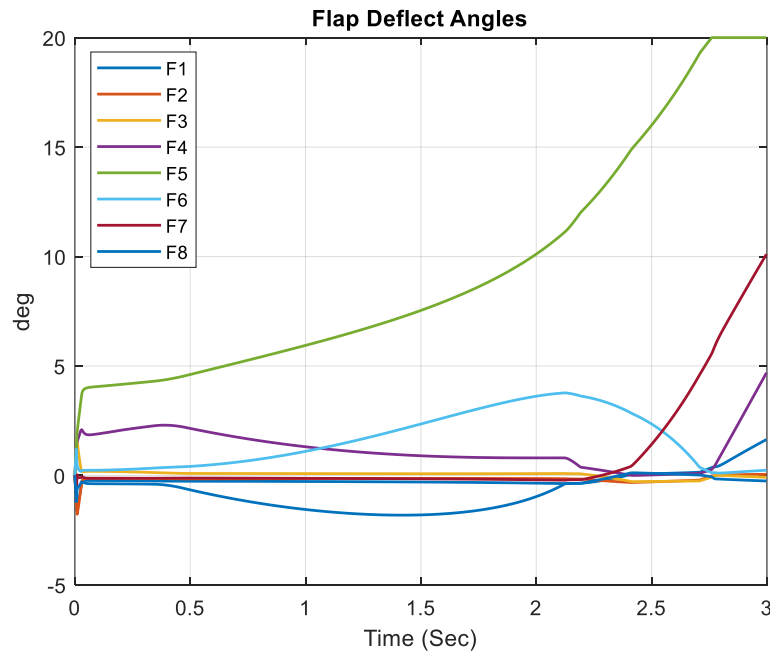


Figure 23 – NDI test flap deflection angles

The simulation results for the INDI open loop test are shown in Figure 24 through Figure 26. It is apparent that the initial transient is different than the NDI results. Rather than going directly to the commanded acceleration, there are oscillations in the response before the acceleration converges to the commanded values. This is due to the fact that INDI relies on the filtered state feedback signals so it requires time to converge on the correct solution. The duration of these oscillations is short and the algorithm successfully functions as expected following the startup transient.

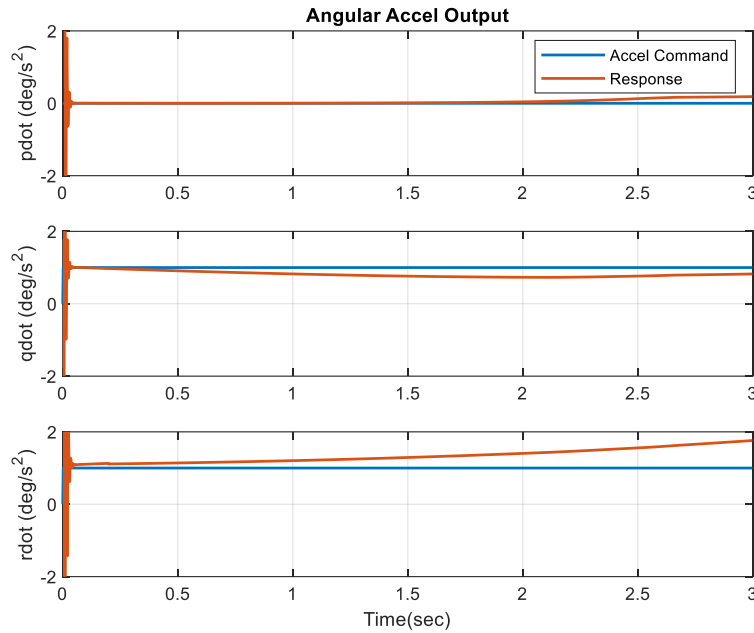


Figure 24 – INDI test acceleration outputs

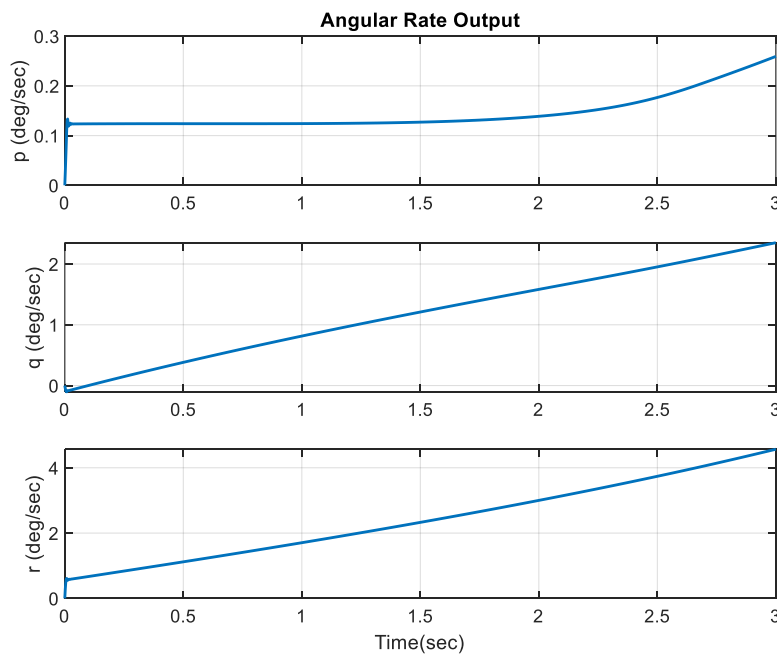


Figure 25 – INDI test rate output

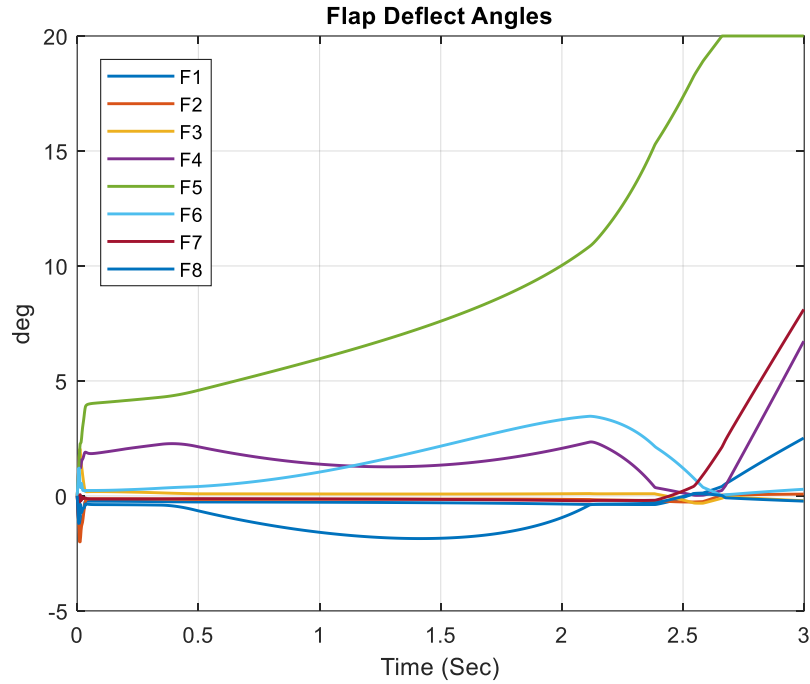


Figure 26 – INDI test flap deflection angles

The simulation results show that the NDI and INDI dynamic inversion schemes function as expected. At first glance it appears that the NDI scheme has better performance with a better startup transient and lower steady state error. However, for these tests perfect modeling knowledge was used in the controller. The effect of parameter uncertainties is evaluated in a later section.

#### 4.1.2 Rate Controller

The step response for the closed loop rate controller is shown on Figure 27. The response for both NDI and INDI inversion schemes are plotted and overlayed for comparison. The results show that both methods respond to the pitch and yaw rate steps while maintaining a small roll rate. One of the key benefits of utilizing dynamic inversion is the decoupling of the control axes. The NDI results show that there is virtually no effect on the roll axis from commanding pitch and yaw. The INDI results show an initial response in the roll axis from the commands, but it is quickly eliminated and the roll axis errors remain small.



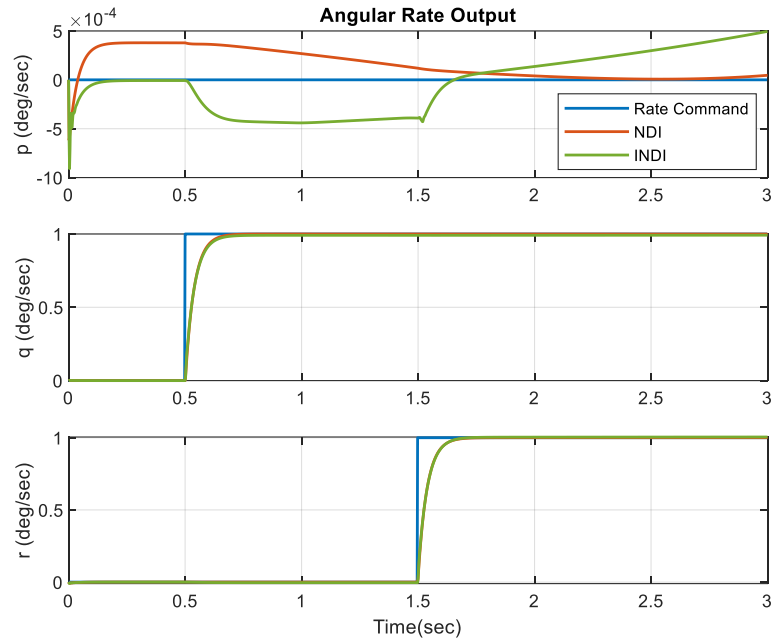


Figure 27 – Rate control performance

Figure 28 displays the flap deflections for the two sets of results. Both plots show similar deflection inputs as expected. Spikes can be seen in the commanded deflections when the step inputs are issued and the deflections continue to vary as the vehicle rotates.

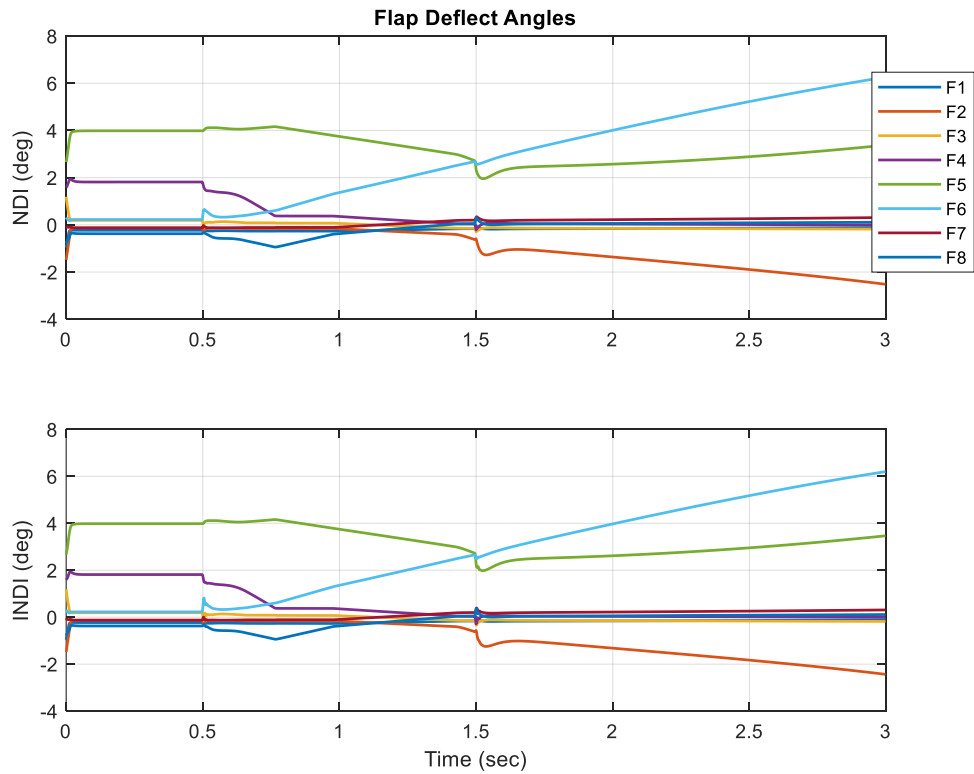


Figure 28 – Rate control test flap deflections

### 4.1.3 Angle Controller

Figure 29 and Figure 30 plot the closed loop step response for the angular displacement controller using the two dynamic inversion schemes. Step commands of 1 degree are issued to the vehicle angle of attack and sideslip angle. In both cases the control system responds as expected to the commands. A small amount of coupling can be seen in the bank angle. This coupling is to be expected since the dynamic inversion process is only applied to the vehicle body axis rotations, which do not translate directly to the bank, angle of attack, and sideslip angles. Nevertheless, the proportional controller quickly eliminates the induced bank angle error.

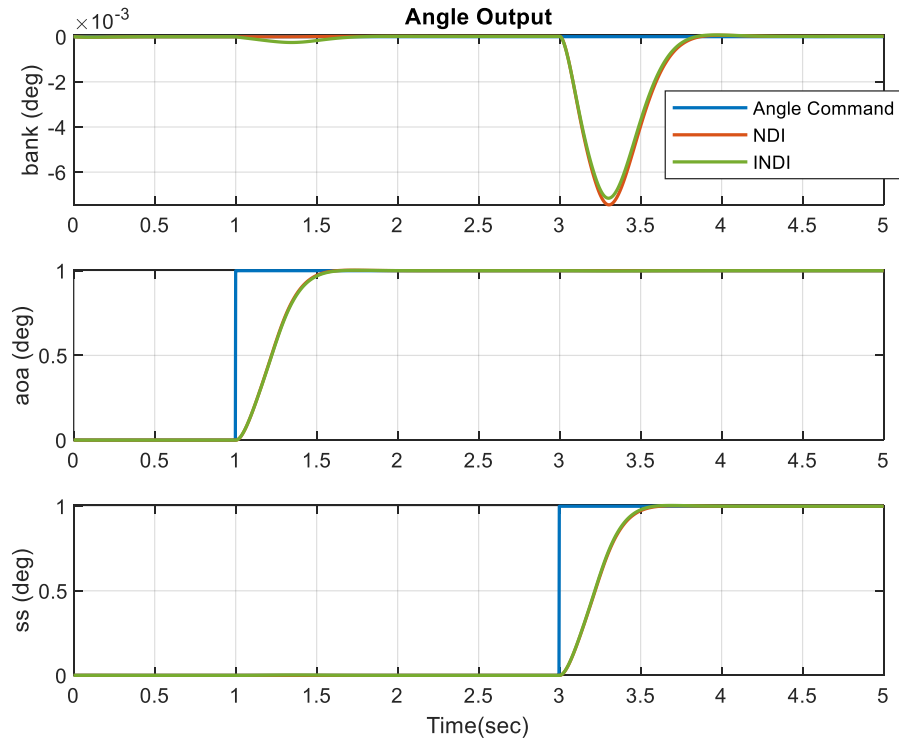


Figure 29 – Angle control performance

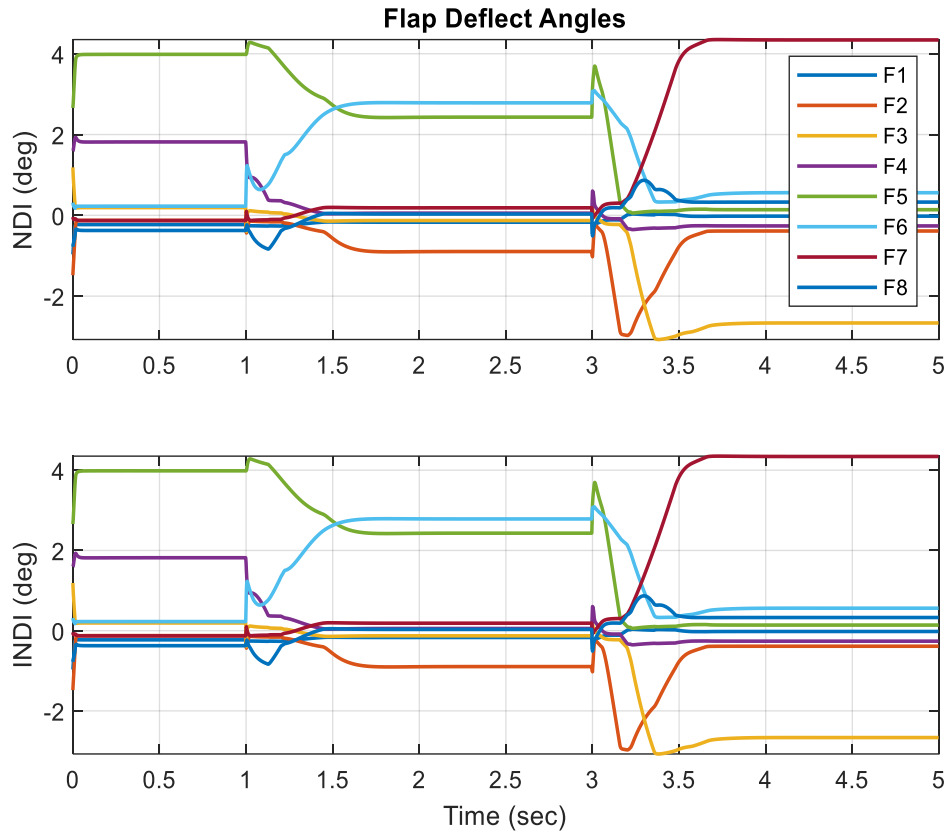


Figure 30 – Angle control test flap deflections

This concludes the analysis of the controller rate and angle control loops. The NDI and INDI control methods both show that they are successful in responding to the commanded rotations.

## 4.2 Guidance Law

This section presents the results for the closed loop system with the guidance law active. The initial test checks that the control system successfully holds the commanded flight path angle and heading angle constant. The simulation initializes with a flight path angle of  $-5.5^\circ$  and a heading angle of  $0^\circ$ . The vehicle is commanded to hold those initial conditions constant throughout the test. To assess the robustness of the controller, the angle of attack and side slip angle are initialized at zero and must rotate to the correct positions which will induce some initial error in the response.

The results for the constant command test are presented in Figure 31 through Figure 33. Figure 31 plots the flight path angle and heading angle response for NDI and INDI. Both control schemes successfully hold the commanded velocity vector direction constant as expected. The NDI response shows a larger steady state error, although this error is still extremely small. The error in NDI can be attributed to slight mismatches between the interpolated aerodynamic model data used in the control law and the true model data.

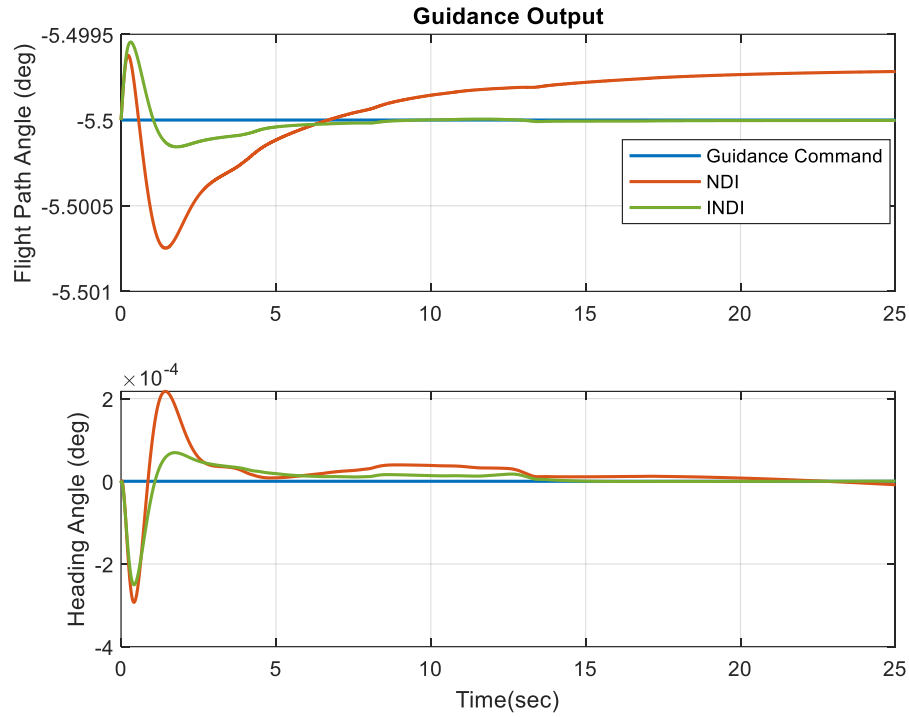


Figure 31 – Guidance law response to constant inputs

Figure 32 plots the angular displacements commanded by the guidance law and the control system response. In both cases, the control system successfully track the commanded pitch and yaw angles while keeping the bank angle relatively small.

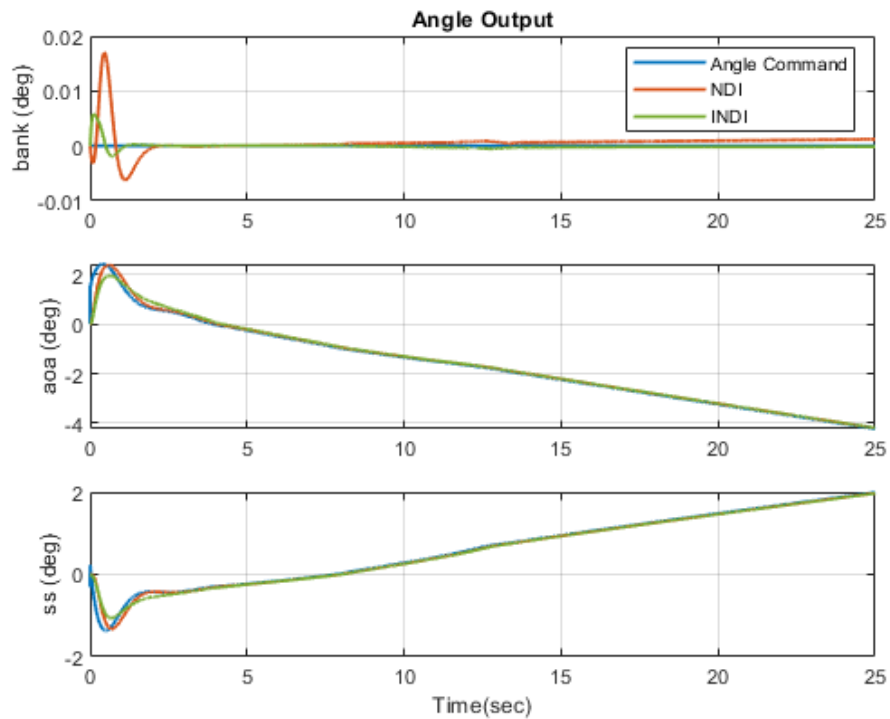


Figure 32 – Angle response to constant guidance inputs

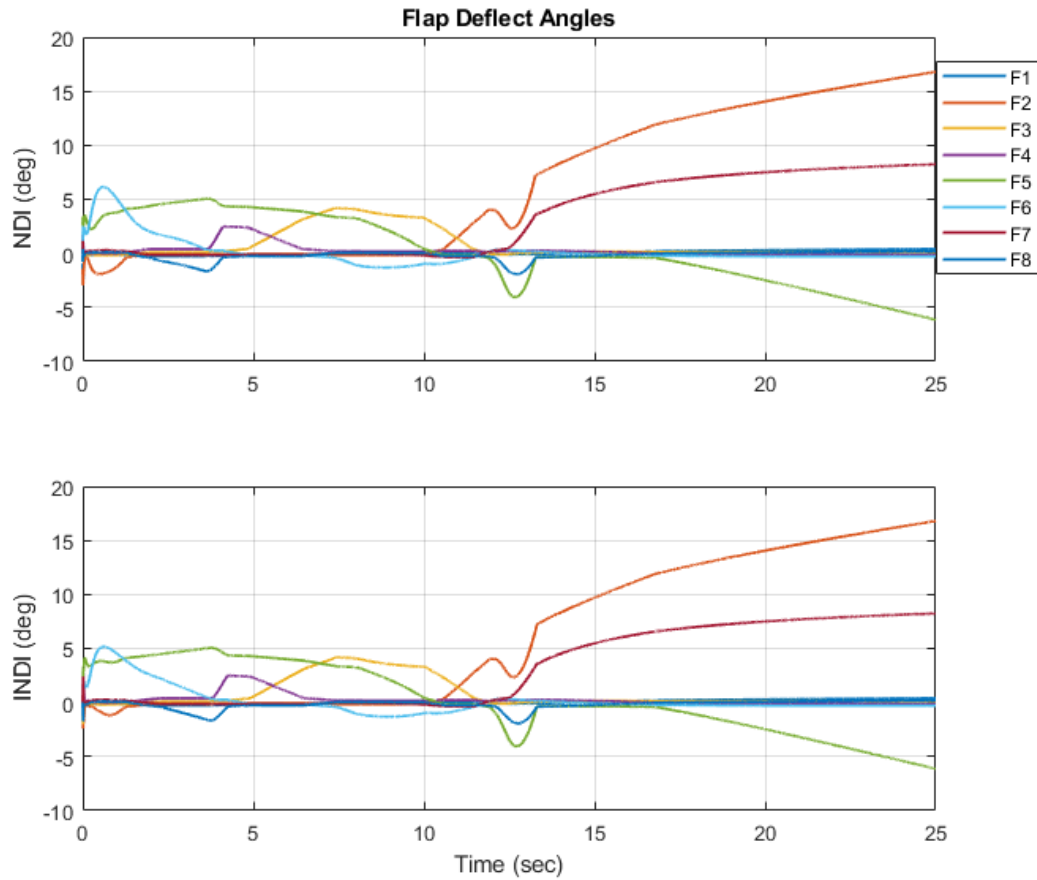


Figure 33 – Flap deflection angles for constant guidance input

The second test scenario initializes with a flight path angle of -5.5 degrees and heading angle of 0 degrees. Beginning at time zero, a ramp input is commanded to the flight path angle for 10 seconds. Following this, the flight path angle is held constant and a ramp input is commanded to the heading angle. The results for this test are shown in Figure 34 through Figure 36. Both NDI and INDI schemes are shown to successfully track the ramp inputs.

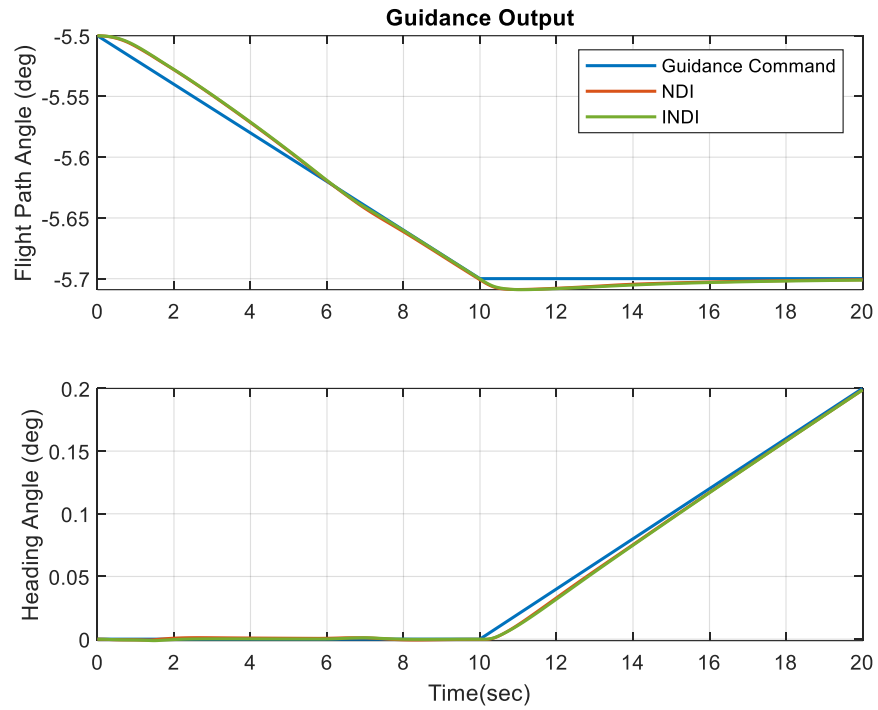


Figure 34 – Guidance law response to ramp inputs

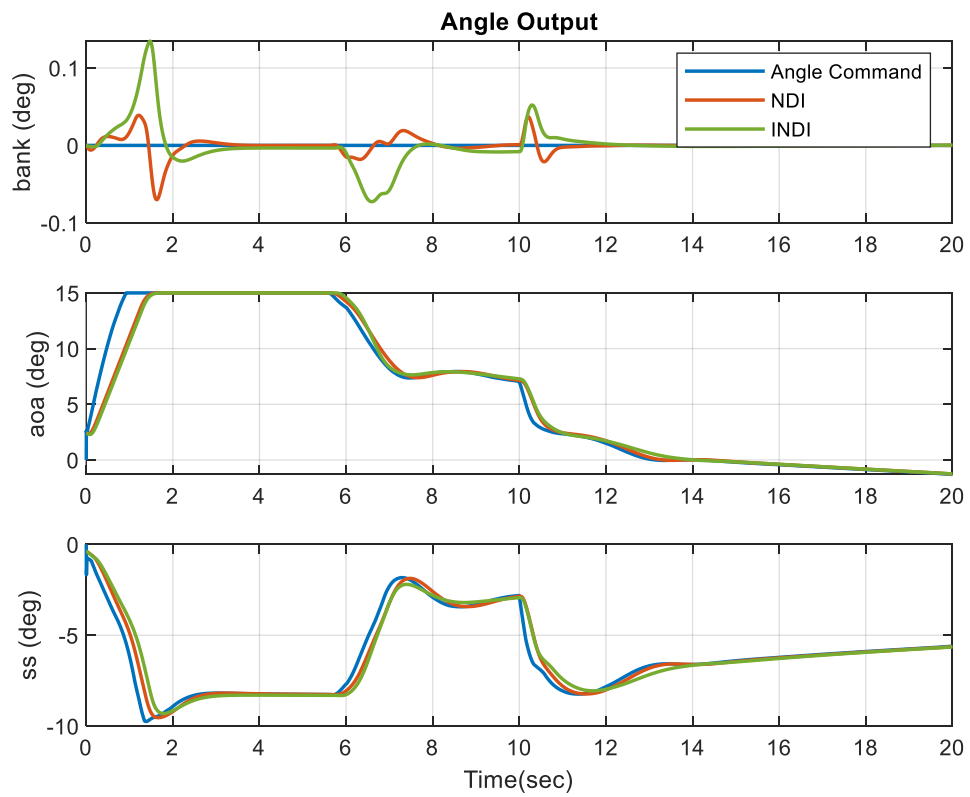


Figure 35 – Angle response to guidance ramp inputs

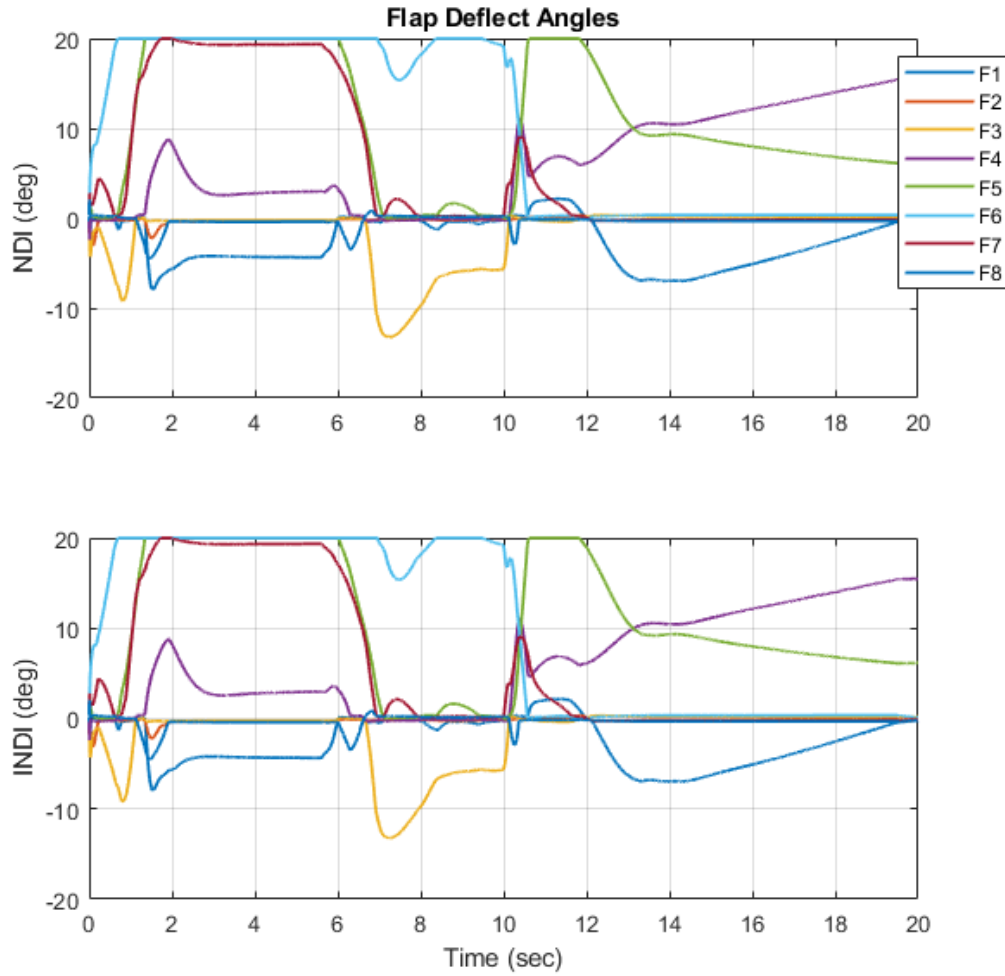


Figure 36 – Flap deflection angles for guidance ramp input

### 4.3 Flight Condition Variation

To further assess the robustness of the controller, the control system was tested under various initial flight conditions. Due to the implementation of dynamic inversion, changes in flight conditions should have minimal impact on system performance. This is because changes in plant dynamics are handled automatically by the inversion loops. A total of nine cases were executed with the same angle of attack and sideslip angle command profile. Case 5 represents the baseline conditions that the command profile was derived from. These initial conditions for each case are defined in Table 9.

Table 9 – Flight condition test case summary

| Case Number  | Initial Mach Number | Initial Altitude (km) |
|--------------|---------------------|-----------------------|
| 1            | 20                  | 80                    |
| 2            | 20                  | 100                   |
| 3            | 20                  | 120                   |
| 4            | 30                  | 80                    |
| 5 (baseline) | 30                  | 100                   |
| 6            | 30                  | 120                   |
| 7            | 40                  | 80                    |
| 8            | 40                  | 100                   |
| 9            | 40                  | 120                   |

The results for the nine scenarios are plotted in Figure 37 below. Since the performance of NDI and INDI have been shown to be near identical, only the INDI results are presented. The results show that the flight conditions have minimal impact on the controller performance as expected. Figure 38 plots the range of velocities and altitudes covered by the test cases.

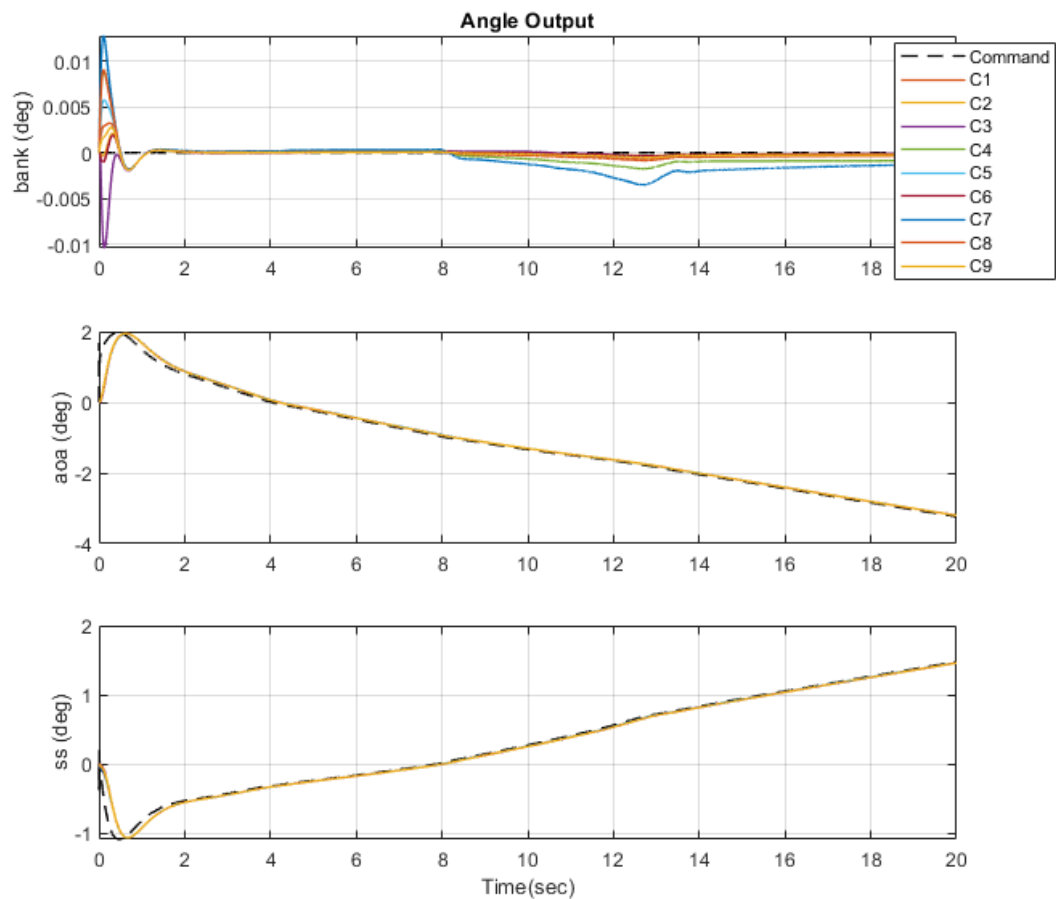


Figure 37 – Flight condition variation test results



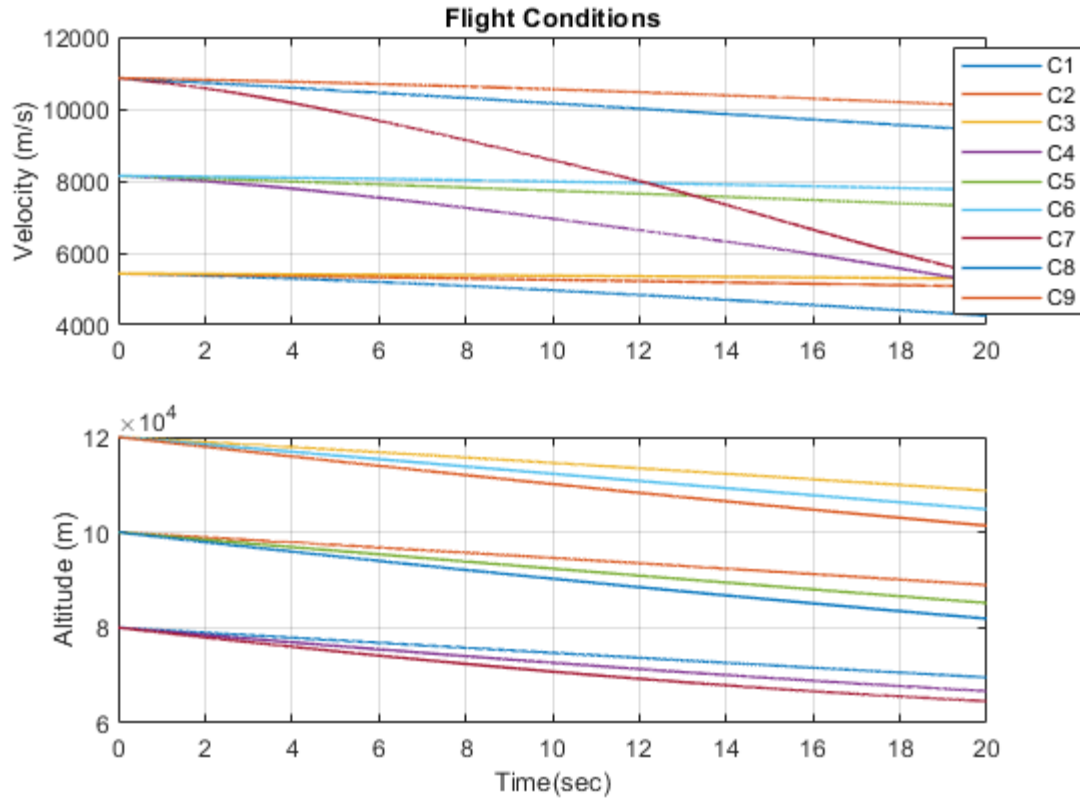


Figure 38 – Flight condition velocity and altitude profiles

#### 4.4 Parameter Uncertainty

The NDI and INDI processes both utilize some level of modeling knowledge to compute forces and torques. The simulation results presented in the previous sections utilized near-perfect modeling knowledge in the controller. To assess the effect of modeling uncertainty, a 10% error factor is applied to the aerodynamic force and moment coefficients.

Figure 39 plots the guidance law results with the 10% error factor applied using the NDI control law. The test setup is the same as the constant flight path angle test described in section 4.2, and the results from that test are overlayed as a baseline. It is clear from Figure 39 that the error factor has a noticeable effect on the NDI system performance. There is a significant increase in the flight path angle error when including the error factor. This is due to the NDI method's reliance on model parameters and should be taken into account when implementing the control law.

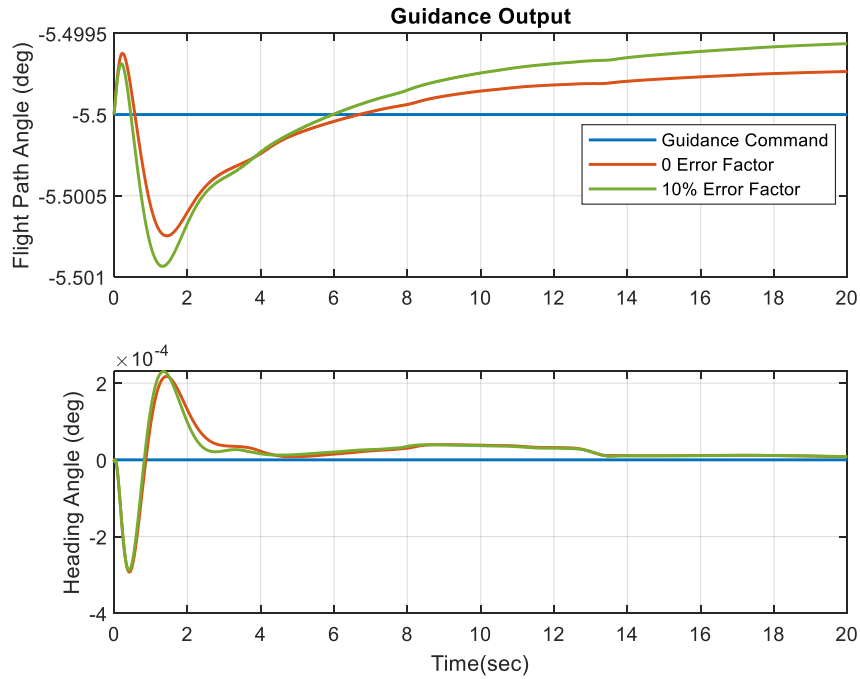


Figure 39 – NDI parameter uncertainty test

The results from the INDI control law are plotted in Figure 40. The results show that the effects of the error factor on the INDI control law are negligible. These results are expected since the INDI replaces the plant dynamics model with state feedback in the controller. This makes the INDI control law less prone to performance loss due to modeling errors which is a strong advantage of utilizing the method.

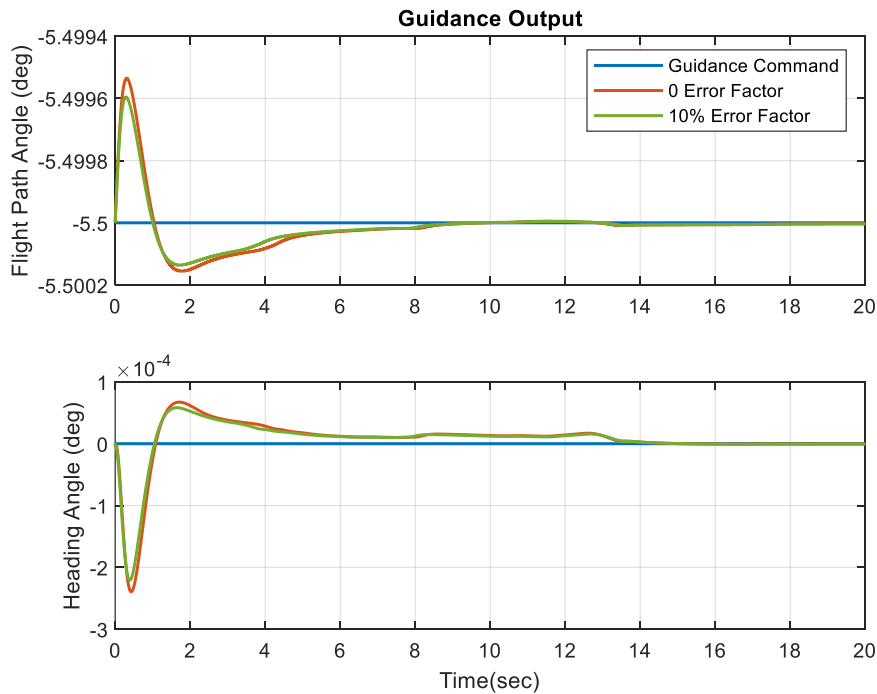


Figure 40 – INDI parameter uncertainty test

## 5 Conclusion & Recommendations

This concludes the design and analysis of the aerodynamic flap control system for a hypersonic re-entry vehicle. The dynamic inversion based control system has been proven to be capable of stabilizing and controlling the vehicle trajectory throughout a range of flight conditions. The two inversion schemes analyzed show similar performance when model uncertainties are small, but NDI performance is shown to suffer more as the uncertainty magnitude increases. In both cases, the dynamic inversion control methodology is shown to be an effective approach to control the deployable re-entry vehicle design.

There are steps that can be taken to improve the accuracy of the system dynamics model. All state feedback utilized in the simulation was fed directly from the state variables without any additional sensor noise or error modeling. To improve the fidelity of the model, sensor modeling should be included to assess the effect that these factors have on the control system performance. It is likely that this will have a larger effect on the INDI method due to its reliance on state feedback. The addition of noise may require additional tuning of the filter as well. Additionally, it should be assessed if there are any vehicle bending modes that could affect control system performance. This may require additional bending mode filters to be implemented in the control law.

After improving the modeling fidelity, the controller should be tuned to meet a realistic set of control requirements. Requirements such as rise time, accuracy, and stability margins should drive controller design. The implementation of dynamic inversion effectively transforms the highly nonlinear plant into simple integrator which greatly simplifies the design of the feedback control loops. This factor can be leveraged when designing these control loops to meet requirements.

Lastly, the control system should be verified by testing realistic flight profiles. The analysis presented in this report was limited in that it did not include a method of generating realistic flight path angle and heading angle profiles over the course of an entire flight. The control system was shown to be capable of responding to commands over a wide range of flight conditions, but this should be taken further to include full flight profiles and edge cases. This will further provide confidence that the control method is suitable for the intended mission.

## References

- [1] Margolis, B., Okolo, W., Nikaido, B., Barton, J., D'Souza, S., "Control and Simulation of A Deployable Entry Vehicle With Aerodynamic Control Surfaces", AIAA Entry, Descent, and Landing GN&C Technology IV, 2019.
- [2] Sepulveda, J., "Aerodynamic Modeling and Assessment of Flaps for Hypersonic Trajectory Control of Blunt Bodies", University of Illinois Master's Thesis, 2017.
- [3] Dsouza, S. N., Okolo, W., Nikaido, B., Yount, B., Tran, J., Margolis, B., Smith, B., Cassell, A., Johnson, B., Hibbard, K., Barton, J., and Hays, Z., "Developing a Feasible Flap Control Design for Lifting Nano-ADEPT," AIAA Aviation Forum, 2019.
- [4] Vant't Veld, R., "Incremental Nonlinear Dynamic Inversion Flight Control Stability and Robustness Analysis and Improvements", Delft University Master's Thesis, 2016.
- [5] Cassell, A., "Deployable Entry Vehicles for Future Science and Exploration Missions", Bulletin of the American Astronomical Society, 2021.
- [6] Venkatapathy, E., "Ballistic and Lifting Nano ADEPT – Flight Testing for Mission Infusion Opportunities", OPAG Briefing, August 2016.
- [7] Smith, B., Yount, B., Kruger, C., Brivkalns, C., Makino, A., Cassell, A., Zarchi, K., Mcdaniel, R., Ross, J., Wercinski, P., Venkatapathy, E., Swanson, G., and Gold, N., "Nano-ADEPT aeroloads wind tunnel test," IEEE Aerospace Conference, 2016.
- [8] Cruz, J., Green, J., "Subsonic Dynamic Testing of a Subscale ADEPT Entry Vehicle", NASA Langley Research Center, AIAA Aviation Forum, 2019.
- [9] Dsouza, S. N., "Pterodactyl: Integrated Control Design for Precision Targeting of Deployable Entry Vehicles", NASA Ames Research Center, Interplanetary Probe Workshop, 2018.
- [10] Vinh, N., Busemann, A., Culp, R., "Hypersonic and Planetary Entry Flight Mechanics", The University of Michigan Press, 1982.
- [11] Wang, Y., Sheu, D., Lin, C., "A Unified Approach to Nonlinear Dynamic Inversion Control with Parameter Determination by Eigenvalue Assignment", Mathematical Problems in Engineering, 2015.
- [12] Wang, X., Kampen, E., Chu, Q. "Stability Analysis for Incremental Nonlinear Dynamic Inversion Control", AIAA Guidance, Navigation, and Control Conference, 2018.
- [13] Lombaerts, T., Kaneshige, J., Schuet, S., Hardy, G., Aponso, B., Shish, K., "Dynamic Inversion based Full Envelope Flight Control for an eVTOL Vehicle using a Unified Framework, AIAA SciTech Forum, 2020
- [14] Ola Harkegard  
(2022). QCAT (<https://www.mathworks.com/matlabcentral/fileexchange/4609-qcat>), MATLAB Central File Exchange. Retrieved March 22, 2022.